Crack Detection in Silicon Wafers Using Shearography

Ramak Motamedi

A Thesis

In The department

Of

Mechanical and Industrial Engineering

Presented in Partial Fulfillment of the Requirements
for the Degree of Master of Applied Science (Mechanical Engineering) at
Concordia University
Montreal, Quebec, Canada

September 2008

© Ramak Motamedi, 2008

Library and Archives Canada

Published Heritage Branch

395 Wellington Street
Ottawa ON K1A 0N4
Canada

Bibliothèque et Archives Canada

Direction du Patrimoine de l'édition

395, rue Wellington
Ottawa ON K1A 0N4
Canada

Your file Votre référence
ISBN: 978-0-494-45495-4
Our file Notre référence
ISBN: 978-0-494-45495-4

NOTICE:
The author has granted a non-exclusive license allowing Library and Archives Canada to reproduce, publish, archive, preserve, conserve, communicate to the public by telecommunication or on the Internet, loan, distribute and sell theses worldwide, for commercial or non-commercial purposes, in microform, paper, electronic and/or any other formats.

AVIS:
L'auteur a accordé une licence non exclusive permettant à la Bibliothèque et Archives Canada de reproduire, publier, archiver, sauvegarder, conserver, transmettre au public par télécommunication ou par l'Internet, prêter, distribuer et vendre des thèses partout dans le monde, à des fins commerciales ou autres, sur support microforme, papier, électronique et/ou autres formats.

The author retains copyright ownership and moral rights in this thesis. Neither the thesis nor substantial extracts from it may be printed or otherwise reproduced without the author's permission.

L'auteur conserve la propriété du droit d'auteur et des droits moraux qui protège cette thèse. Ni la thèse ni des extraits substantiels de celle-ci ne doivent être imprimés ou autrement reproduits sans son autorisation.

In compliance with the Canadian Privacy Act some supporting forms may have been removed from this thesis.

Conformément à la loi canadienne sur la protection de la vie privée, quelques formulaires secondaires ont été enlevés de cette thèse.

While these forms may be included in the document page count, their removal does not represent any loss of content from the thesis.

Bien que ces formulaires aient inclus dans la pagination, il n'y aura aucun contenu manquant.

ABSTRACT

Crack Detection in Silicon Wafers Using Shearography

Ramak Motamedi

Defects in silicon wafers affect their mechanical stability considerably during their processing and handling. In the new generation of thin silicon wafers, in addition to sub-surface defects, cracks are also one of the most important defects that need to be evaluated. A comprehensive review of literature suggests the use of different techniques for non destructive evaluation (NDE) of silicon wafers. Among the few NDE techniques that can be used for both sub-surface and crack detection, Shearography has the advantage of being a whole field technique that can be utilized as a non-contact method for online inspection.

Although, recently shearography has been used for sub-surface defect detection in silicon wafers, the capability of this technique to identify and detect cracks has not been investigated yet. In this work, a shearography system has been developed for non-destructive evaluation of silicon wafers. The optical set-up was arranged and several experiments were carried out to optimize its performance. Batch of perfect wafers, wafers with sub-surface defects and cracked wafers of 500μm thickness were qualitatively evaluated using the developed system. Two different loading mechanisms were used to stress the silicon wafer and the advantage of uniform thermal loading over concentrated force loading for crack and sub-surface defect detection has been discussed. In addition to crack detection, the unique potential of the developed system for detection of crack propagation has been discussed.

ACKNOWLEDGMENTS

I would like to thank my supervisor, Dr. Narayanswamy Sivakumar, who introduced me to the field of optical metrology. His valuable and encouraging guidance, patience and support throughout this thesis are greatly appreciated.

I would like to thank my co-supervisor, Dr. Suong Van Hoa, for his detailed and constructive comments. His wide knowledge and his logical way of thinking have been of great value for me.

Finally I wish to express my warm and sincere thanks to my parents and my brother for their understanding and endless love. They have always supported and encouraged me to do my best in all aspects of life.

Table of Contents

List of Figures viii

List of Tables xi

Chapter 1 Introduction

1.1 Silicon wafers 1

1.2 Defects in silicon wafers 1

1.3 Defect detection techniques 2

1.3.1 Light scattering 3

1.3.2 Scanning electron microscopy (SEM) 4

1.3.3 Atomic force microscopy (AFM) 5

1.3.4 X-ray diffraction 6

1.3.5 Ultrasonic measurement techniques 7

1.3.6 Thermography 9

1.3.7 Optical transmission 10

1.4 Interferometric techniques for defect detection 11

1.4.1 Holography 12

1.4.2 Speckle pattern interferometry 14

1.5 Motivation for Current work 14

1.6 Objective and scope of the research 16

Chapter 2 Theory of Speckle Interferometry

2.1 Introduction 17

2.2 Speckles 18

2.3 Speckle interferometry 20

2.3.1 Correlation fringes 22

2.3.2 Quantitative analysis of the interferograms 26

2.4 Speckle interferometry techniques 27

2.4.1 Electronic speckle pattern interferometry (ESPI) 27

2.4.2 Shearing speckle interferometry (Shearography) 28

2.5 Applications of shearography in NDE 30

2.6 Summary 33

Chapter 3 Shearography Optical Set-up

3.1 Introduction 34

3.2 Basic arrangement of the optical set-up 34

3.3 Selection criteria of the optical set-up components 35

3.3.1 The illumination system 36

3.3.2 The Shearing system 39

3.3.3 The imaging system 41

3.3.4 The recording system 42

3.3.5 The image processing system 44

3.3.6 The mechanical system for applying load 46

3.4 Summary 48

Chapter 4 Results and Discussion

4.1 Introduction 49

4.2 Optical set-up optimization 49

4.2.1 Optimal speckle size 49

4.2.2 Correlation fringe formation 51

4.2.3 Surface slope measurement 55

4.3 Non-destructive evaluation of silicon wafers 64

4.3.1 Crack detection on silicon wafers 64

4.3.2 Extension for crack propagation detection in silicon wafers 70

4.3.3 Sub-surface defect detection in silicon wafers 71

4.4 Summary 73

Chapter 5 Conclusion

5.1 Conclusion 74

5.2 Future works 76

REFERENCES 77

APPENDIX 1

List of Figures

Figure 1.1	Schematic of a light scattering optical set-up	4
Figure 1.2	Schematic of a scanning electron microscope	5
Figure 1.3	Schematic of an AFM configuration	6
Figure 1.4	Optical set-up configuration for X-ray topography	7
Figure 1.5	Schematic of a scanning acoustic microscope	8
Figure 1.6	Schematic of RUV set-up	9
Figure 1.7	Schematic of a lock-in ultrasound thermography set-up	10
Figure 1.8	Schematic of an optical transmission set-up	11
Figure 1.9	Shearographic fringe pattern of a sub-surface defect in a material	12
Figure 1.10	Schematic of a holography set-up for NDT technique	13
Figure 1.11	Schematic of the speckle interferometry set-ups	14
Figure 2.1	Speckle pattern of a rough surface (Al plate) illuminated with laser	18
Figure 2.2	Speckle configurations	19
Figure 2.3	Correlation fringe patterns	26
Figure 2.4	ESPI optical set-ups	28
Figure 2.5	A Michelson-type shearing speckle interferometer	29
Figure 2.6	Defect detection in different materials using shearography	32
Figure 2.7	Fringe patterns of a phantom specimen with abnormal areas	32
Figure 2.8	Shearography fringe pattern of a silicon wafer with sub-surface defects	33
Figure 3.1	The schematic of the shearography optical set-up	35
Figure 3.2	The functional components of the shearography optical set-up	36
Figure 3.3	Schematic of a spatial filter configuration	38

Figure 3.4 Lateral shearing for spherical wavefront 39

Figure 3.5 The shearing system: Michelson-interferometer 40

Figure 3.6 Working distance and inspection area shown schematically in our shearography set-up 41

Figure 4.1 Various appearance of inappropriate speckle patterns 51

Figure 4.2 Subtraction of inappropriate speckle patterns and resulting fringe patterns 51

Figure 4.3 Shearography fringe patterns resulted from subtraction of speckle patterns after different center-displacement of the Al plate 53

Figure 4.4 Shearography fringe patterns after different center-displacement of the Al plate 53

Figure 4.5 Shearography fringe patterns after different center-displacement of the carbon composite plate 54

Figure 4.6 Optical arrangement of a shearography set-up for normal-illumination 56

Figure 4.7 Speckle pattern with a noise spot 57

Figure 4.8 Schematic of re-arranged set-up for normal illumination 57

Figure 4.9 Silicon wafer surface roughness 58

Figure 4.10 Shearography fringe patterns from a normal illumination set-up after different center-displacement of the silicon wafer 58

Figure 4.11 Shearography fringe pattern after performing electronic noise filtering 59

Figure 4.12 3-D plot of phase variation of the deformed silicon wafer obtained by Fourier transformation 60

Figure 4.13 Phase variation on central cross-section of the deformed silicon wafer obtained by Fourier transformation 61

Figure 4.14 Out-of-plane displacement gradient of the center cross section of the silicon wafer obtained from low pass-filtered unwrapped phase map 62

Figure 4.15 Comparison between the theoretical out-of-plane displacement gradient of the silicon wafer and the shearography result 63

Figure 4.16 Fringe patterns of a perfect wafer obtained by thermal loading 66

Figure 4.17 Fringe patterns of a cracked wafer obtained by thermal loading 67

Figure 4.18 Fringe patterns of a cracked wafer obtained by concentrate-force loading 68

Figure 4.19 Schematic of the fracture angle in a (100) silicon wafer 69

Figure 4.20 Fringe patterns of a broken wafer obtained by thermal loading 70

Figure 4.21 Fringe patterns of a silicon wafer with sub-surface defect obtained by thermal loading 72

List of Tables

Table 3.1 Different lasers that can be used for a shearography set-up 36

Table 3.2 Specifications and spectral response of CV-A11 44

Chapter 1 Introduction

1.1 Silicon wafers

Silicon wafers are extensively used in the semiconductor industries and microelectronic applications. With recent work in alternative energy sources, the solar industry is also one of the main consumers of the silicon for producing solar cells and panels economically. To balance the rising cost of silicon and also due to the fact the silicon surface is only of importance; now the silicon wafers are produced with the thickness of 100μm which are much thinner than the previous wafers with the thickness of 600μm [1]. This methodology for making the wafers decreases the efficiency of the manufacturing systems because of the developing cracks in the wafers, due to their thin thickness, and consequently their breakages. The critical mechanical stresses that may cause the thin wafers breakage can happen through: wafer handling and processing. The wafers breakages cause the operation line to be shut down for cleaning up the tools and fixtures. In addition to the time-consuming part of the cleaning up the equipment, the wafer slices damage the production equipment which decreases their life time significantly. So, there is an inevitable need for inspecting the silicon wafers while manufacturing to avoid loss due to wafer breakages.

1.2 Defects in silicon wafers

Silicon wafers breakage can occur due to crack defects and also inherent defects which are created during its crystal growth. In the new thin silicon wafers, cracks are one of the

most important defects. Cracks can appear in the wafers during wafer sawing or laser cutting. These cracks can propagate in the wafer through the post-processing of the wafers, such as the process of antirefleting coating, front and back contact firing and soldering of contact grid, in case of solar silicon wafers [2]. Crystal originated pits (COPs), surface metals, oxide precipitates, hydrogen-induced defects and process-induced defects are some of the most common types of the surface and sub-surface defects in silicon wafers in addition to cracks [3]. Since these defects affect the symmetry of the wafer plane under the loading procedures, they can also cause extra stress on the wafer. Thus, detecting the size and location of these types of defects also help to prevent the use of defective wafers in the processing.

1.3 Defect detection techniques

There are several techniques that are currently in use for defect detection in silicon wafers, like light scattering, scanning electron microscopy (SEM), atomic force microscopy (AFM), x-ray diffraction, ultrasonic measurement techniques, thermography, optical transmission and interferometric techniques. Some of these techniques like light scattering, SEM and AFM can be used only for surface cracks and surface defects. While the other techniques such as x-ray diffraction, ultrasonic measurement techniques, thermography and interferometric techniques can be used for both surfaces (including cracks) and subsurface defects. A method like optical transmission can only be used for crack detection. In next section, an overview of these techniques and their applicability to silicon wafer inspection has been discussed briefly.

1.3.1 Light scattering

Light scattering method is one of the most common and simple techniques that have been used for defect detection of silicon wafers. This technique is based on the change of the light intensity of the scattered light due to its interaction with the diverse microconstructions of a rough surface [4]. In this method, the sample surface is illuminated with the laser light and the scattered light is recorded by a detector. The intensity distribution of the scattered light provides the information of the surface profile. An unexpected change of light intensity would happen when the light scatters from defects and the defects can be identified through the interpretation of the intensity based map.

Okamoto *et al.* have developed a laser scattering system to detect 30-40nm particles on silicon wafers [5]. They use a 266-nm solid-state continuous-wave laser to increase the sensitivity of this detection method. This optical set-up is shown in Figure 1.1(a). The wafer surface is illuminated by the laser light from two different angles. The wafer is both rotated and moved in order to be scanned without moving the laser. The scattered laser-light is gathered by four detectors positioned at four different places. By comparing the light intensity of the scattered light from two illuminating angles, the particles and defects on the wafer surface can be distinguished (Figure 1.1(b) and 1.1(c)).

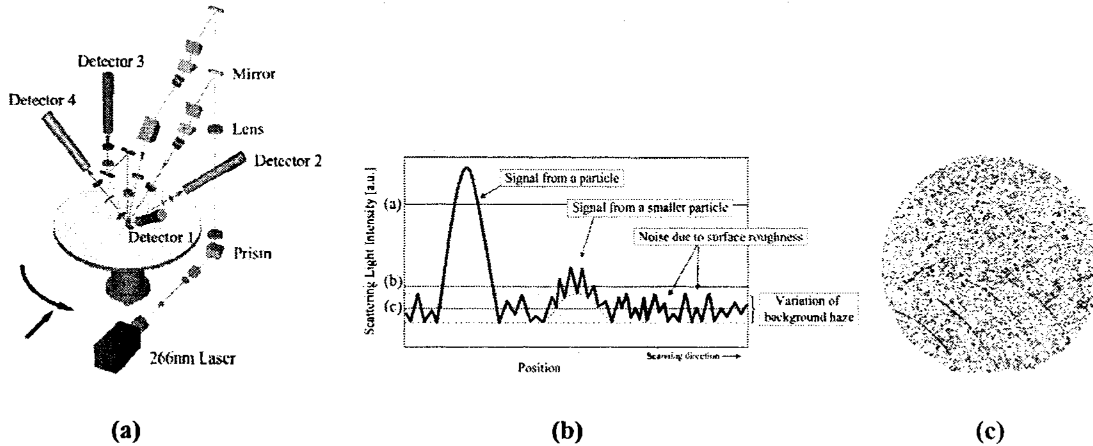

Figure 1.1 (a) Optical set-up of the 30-40nm particles detection system, (b) Light scattering signal obtained from line scanning the wafer surface and (c) Macro scratches observed by laser scattering system [5]

1.3.2 Scanning electron microscopy (SEM)

In SEM, a high-energy beam of electrons impinges on the sample surface, as shown in Figure 1.2(a), and the ejected electrons are sensed by a detector. The SEM image shows the intensity distribution of the emitted signals from the scanned surface [6]. SEM is also one of the frequently used methods for defect detection on silicon wafers and several researches have been done in this field [7-8].

Miyazaki *et al.* have used SEM to observe microstructure shapes of COP's on silicon wafers [9]. In their work, after determining the position of COP's on the wafer by the laser particle counter, SEM has been used to irradiate the marked area by its electron beam. This irradiation causes the area to become resistant to etching by SC-1 and so, during the wafer cleaning the marked area will be shaped as a hill on surface. Figure 1.2(b) shows the SEM image of their work which demonstrates a single and double-type COP on a mirror-polished wafer.

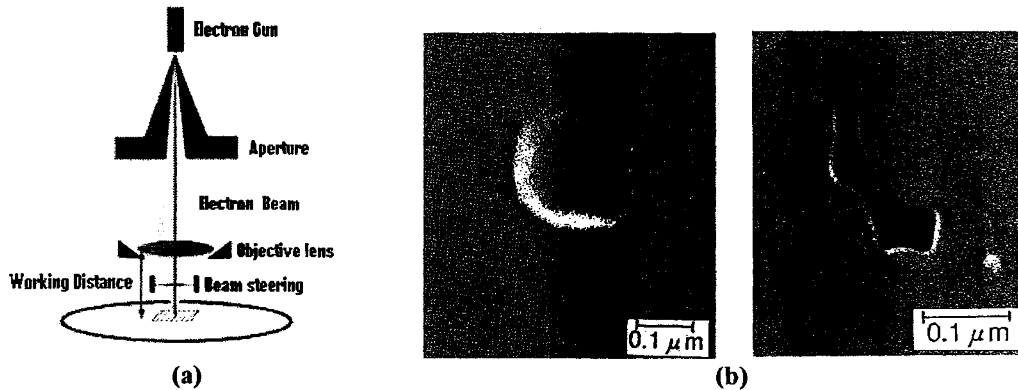

Figure 1.2 (a) Schematic of a Scanning electron microscope [6] (b) SEM image of a single and double-type COP [8]

1.3.3 Atomic force microscopy (AFM)

The AFM principle is based on measuring the deflection of a microcantiliver which scans the sample surface with a sharp tip at its end. The cantilever deflection is usually measured by a laser point reflected from its tip and sensed by the photodiodes [10].

Kobayashi *et al.* have used AFM as a coordinate linked method with a laser scattering system to monitor directly the surface defects of an immersed silicon wafer in slightly Cu-contaminated water [11]. Since the defects that are generated on the wafer surface are too tiny to be observed accurately by laser scattering technique, they have used the AFM to image more precisely the area of defects. By using a highly sensitive laser scattering system, they detect the defects that are equal to or larger than 50nm and then, the detected defect regions are imaged with AFM to obtain the real image of the defects. Nishimura *et al.* have developed an AFM that can directly inspect the whole surface of a 12-in wafer, Figure 1.3. This AFM uses the laser scattering method to characterize the defect shapes [12].

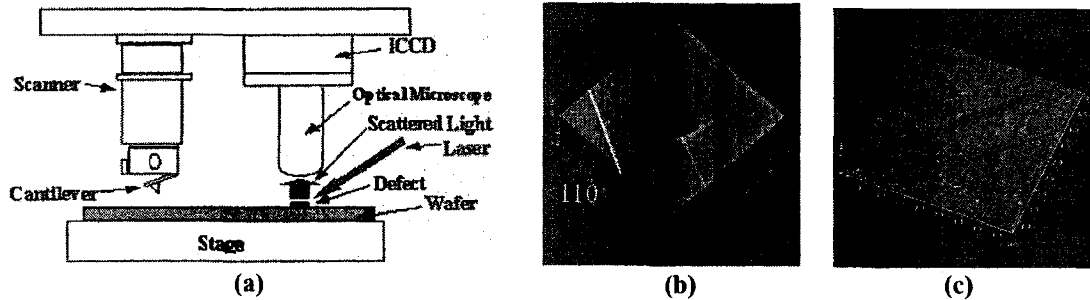

Figure 1.3 (a) AFM configuration to detect defects on a 12-in Si wafer, (b) AFM image of the COP detected on a Si wafer and (c) AFM image of the scratches polished as lines on Si wafer [12]

1.3.4 X-ray diffraction

This technique is based on the diffraction of the x-ray that is scattered from the sample surface. Diffraction happens when the wavelength of the incident wave to a periodic surface is in the range of the repeated distance. Since the wavelength of the x-ray is in angstroms scale and this scale is equal to the atomic distance in crystals, x-rays can be diffracted from the repeating atomic structures in crystalline materials. The intensity distribution of the diffracted x-ray is recorded and it can provide information about the crystallographic structure, physical properties and surface topography of materials [13].

Kawado has reviewed the current development in X-ray diffraction techniques for detection of crystal perfection and surface contamination in large-diameter silicon wafers [14]. Two X-ray testing techniques are usually used to evaluate the wafer surfaces, transmission topography and double-crystal topography, as shown in Figures 1.4(a) and 1.4(b). While the transmission method can be used simply and under easy conditions, the double-crystal topography can be used when more sensitivity for detection of small defect areas is needed. The problem with X-ray topography methods, even the ones

developed for more accurate characterization like plane-wave X-ray topography [15], is the low contrast of their resulting images (Figure 3(c)).

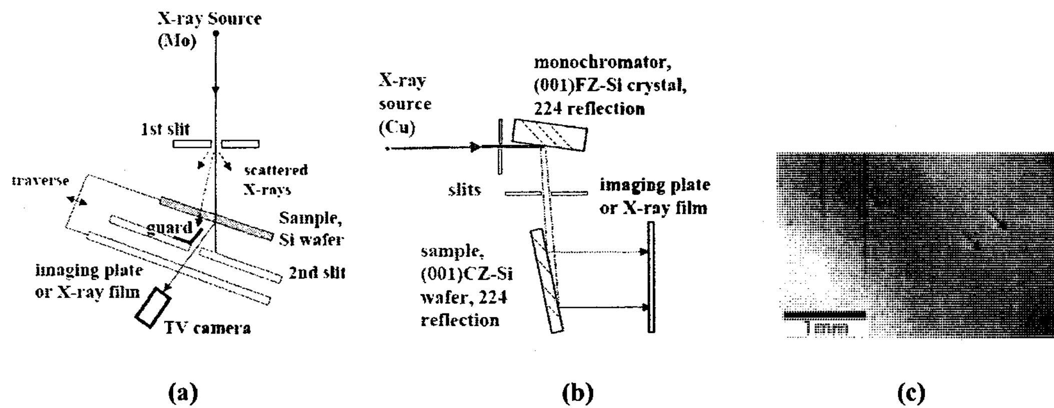

Figure 1.4 (a) Optical set-up configuration for X-ray transmission topography, (b) Example of an optical set-up for double-crystal topography and (c) Microdefects, in an as-grown CZ-Si wafer, detected by plane-wave X-ray topography [14]

1.3.5 Ultrasonic measurement techniques

Scanning acoustic microscopy (SAM): In this technique, the sound waves emitted by an ultrasound transducer hit the sample surface and are reflected by both surface defects and defects inside the material, and boundary surfaces of the sample, as shown in Figure 1.5(a). The change in the acoustic impedance of the all reflected waves compared to those of the reflected waves from the backside surface of the sample will show the material density variation or material discontinuity in the sample. The SAM image is obtained through scanning the entire sample surface. The resolution of the image depends on the frequency of the sound wave. Since the ultrasound wave attenuates in air, a coupling medium, either fluid or vacuum, is needed. The sample will be immersed in coupling medium during the testing time [16].

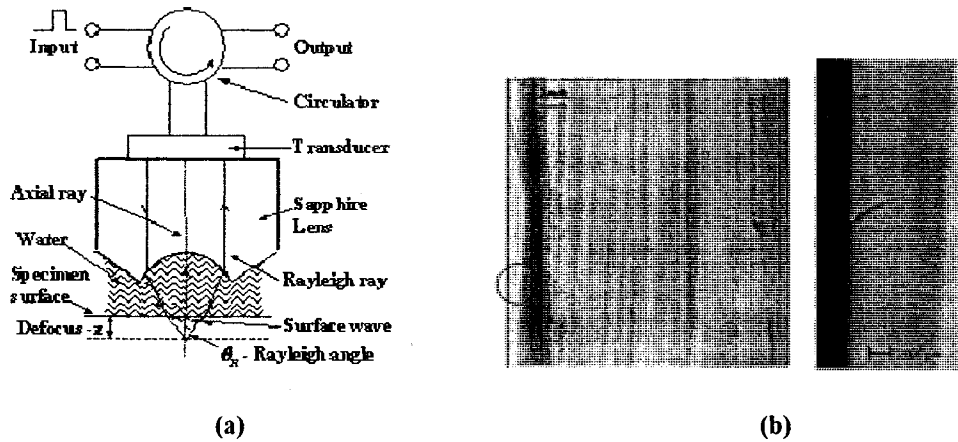

(a) (b)

Figure 1.5 (a) Schematic of a scanning acoustic microscope [16] and (b) SAM image of a silicon wafer with a crack on its edge (left image: zooming area of the crack) [17]

Belyaev *et al.* have inspected silicon wafers by using SAM to detect the periphery microcracks [17]. The wafers have been placed in a tank of deionized water (coupling medium) and the reflected acoustic waves from the front and back surfaces of the wafer was received by the transducer and converted to voltage. The resulting image of the digitized voltage data for the entire silicon wafer was acquired in a few minutes. The accuracy of SAM for crack detection reported in their work is in the range of few micrometers.

Resonance ultrasonic vibrations methodology: Dallas *et al.* have proposed a new technique for crack detection in silicon wafers which was first used to analyze the elastic stress in full-size silicon wafers [1-2]. In this technique, ultrasonic vibrations with adjustable amplitude and frequency were generated by a piezoelectric transducer and applied to the silicon wafer. As it has been shown in Figure 1.6(a), the wafer was coupled to the transducer by applying vacuum to the backside of the wafer. Through transmission of vibrations to the wafer, the acoustic waves were formed at resonance frequencies. An ultrasonic probe was used to scan the surface of the wafer to measure and distinguish the

longitudinal vibration mode on each point of the surface. The Resonance ultrasonic vibrations (RUV) method can detect the cracked wafers by checking their resonance peak amplitude, bandwidth and frequency as shown in Figure 1.6(b). The RUV system can monitor millimeter and sub-millimeter length cracks.

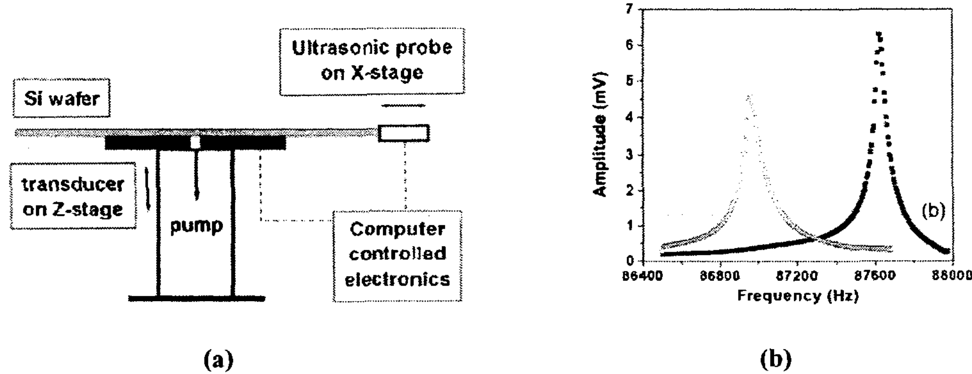

Figure 1.6 (a) Schematic of RUV set-up and (b) RUV parameter variation on a wafer with 6mm crack [1]

1.3.6 Thermography

This method is based on the differences between the thermal conductivity of the defective area compared to that of the perfect areas. Flash lamps or heat lamps are used to heat up the sample surface and the resulting heat distribution over the object surface is detected by an infrared camera. To improve the efficiency of this technique, a new method of ultrasound lock-in thermography (ULT) has been introduced, shown in Figure 1.7, where instead of a thermal source, harmonic vibrations are applied to locally heat the flawed areas with temperature gradient of tens of degrees [18]. However, in order to improve the signal-to-noise ratio, acquiring the images in this technique needs an integration time of some minutes.

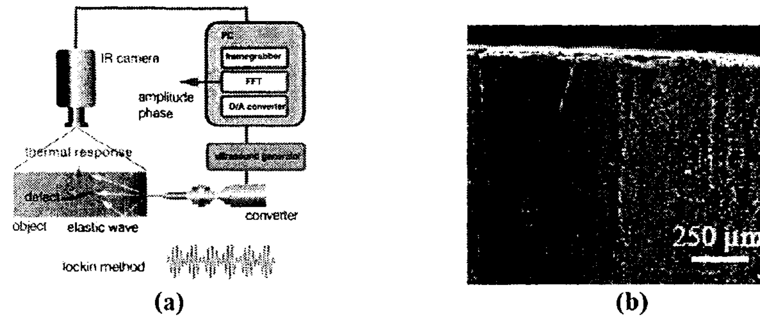

Figure 1.7 (a) Schematic of a lock-in ultrasound thermography set-up [18] and (b) ULT image of a silicon wafer containing a microcrack [19]

Rakotoniaina *et al.* have detected cracks in silicon wafers and solar cells by using lock-in ultrasound thermography [19]. They coupled the wafer to an ultrasound energy transducer through vacuum. Due to the ultrasound excitation, the friction at the perimeter of cracks will generate local heating, which is imaged via the infrared camera. Since the infrared emissivity of the sample surface affect the results considerably, to reduce the wafer transparency to the infrared light, they coat the wafer surface with black paint.

1.3.7 Optical transmission

In this technique, as it has been shown in Figure 1.8, a high intensity flash lamp is placed under the silicon wafer and the flashlight will transmit though the wafer. A CCD camera with an appropriate optical filter is used to capture the image of silicon wafer surface. The width of the cracks that can be detected with this method is determined by the optical diffraction limit which is related to the wavelength of the flash lamp. This method can only detect the cracks which have penetrated through the entire thickness of the wafer.

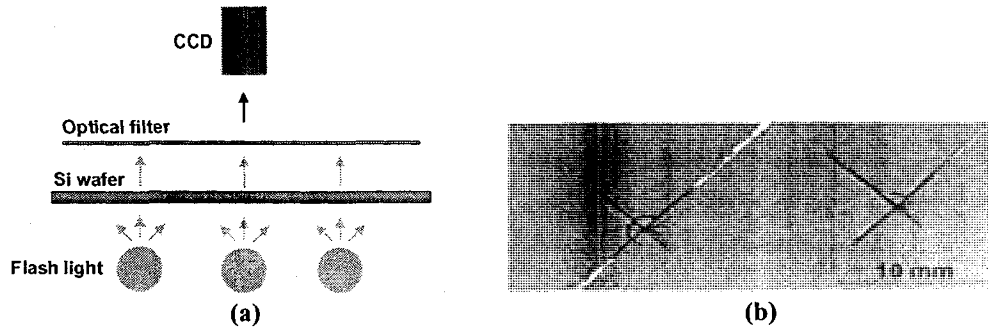

Figure 1.8 (a) Schematic of an optical transmission set-up and (b) an artificial μ-crack detection image in Cz mono-Si with a developed optical transmission system [20]

Rueland *et al.* have detected μ-cracks in silicon wafers and solar cells by using optical transmission method [20]. In their research, an infrared flash-light lamp and a high-resolution CCD camera combined with a blue filter were used. The blue filter was used to detect selectively the cracks with width greater than 1μm since by using this filter, the white light can only be detected by the camera. The final solar cells and the wafers with Al coating on their backside can be inspected by this technique if the crack penetrates to the backside of the coated wafer.

1.4 Interferometric techniques for defect detection

Interferometric techniques are used to visualize or measure the object deformation through determining the phase change of the interfering beams coming from the light source and object surface. Since the defective parts, either due to surface defects or sub-surface defects, show different deformations compared to the perfect parts, the defective areas can be distinguished as anomalies areas in the interference patterns (fringes) as shown in Figure 1.9.

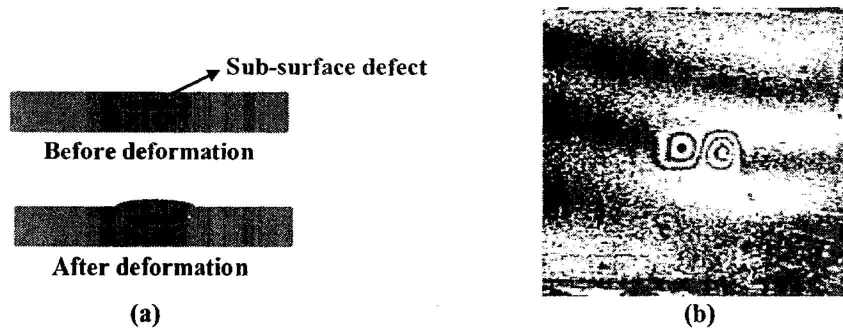

Figure 1.9 (a) Sub-surface defect in a material shown after and before the deformation and (b) shearographic fringe of the 11 mm diameter defect 0.28 mm below the surface of the object [21]

Choosing an appropriate type of loading to deform the object surface and have a sufficient amount of deformation is one of the main parts of any interferometric testing set-up. Thermal loading, pressure (or vacuum) loading, vibrational and concentrate-force (mechanical) loading are the most common methods used for a non-destructive interferometry testing; the choice of which depends on type and size of the defect which is supposed to be detected and the size of the object itself.

The interferometric techniques have the advantage of being full-filed and non-contact compared to other mentioned methods for defect detection. The accuracy of these testing methods is in the range of sub-micrometer. Holographic interferometry and speckle pattern interferometry are the common interferometric methods used for non-destructive evaluation of materials.

1.4.1 Holography

In this method, the laser beam which is scattered by the object surface interferes with a reference beam and the interference pattern is recorded by a detector. A three-

dimensional image of the object can be reconstructed by illuminating the holographic recording (hologram) either with the same reference beam or another one. A holography set-up and a hologram phase data of a mirror containing a scratch has been shown in Figure 1.10. Holography method has a high spatial resolution compared to speckle interferometry techniques, but its high sensitivity to external vibrations has restricted its use in industrial environments [22].

To observe the deformation of an object by holography, a hologram is recorded from the first state of the object. After deforming the object to its second state, an interference pattern can be created by interfering the object beam from its second state and the reconstructed object beam from the hologram of its first state.

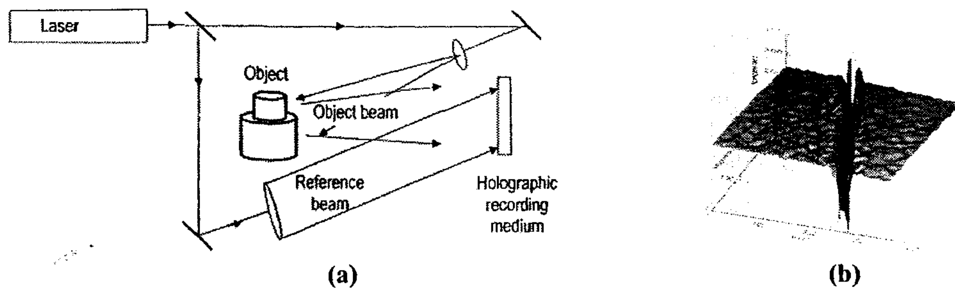

Figure 1.10 (a) Schematic of a holography set-up for NDT technique and (b) hologram phase data of a mirror containing a scratch [23]

Mark *et al.* have used digital holography to detect defects on semiconductor wafers [24]. To have a better spatial resolution for high aspect ratio defects, they have used a laser with a small wavelength (266nm, Deep ultraviolet laser) which can penetrate well inside the tiny defects. By obtaining the phase data with digital holography, they can observe an accurate topology of each defect.

1.4.2 Speckle pattern interferometry

Electronic speckle pattern interferometry (ESPI) and Shearing speckle pattern interferometry (Shearography), shown schematically in Figure 1.11, are the two speckle interferometric techniques that used as non-destructive testing methods [25-27]. These techniques will be explained in detail in chapter 2. Speckle interferometry techniques can be performed much simpler and faster than holography method, however they have lower spatial resolution. Because of its less sensitivity to ambient vibrations, shearography is of more interest in industrial environment.

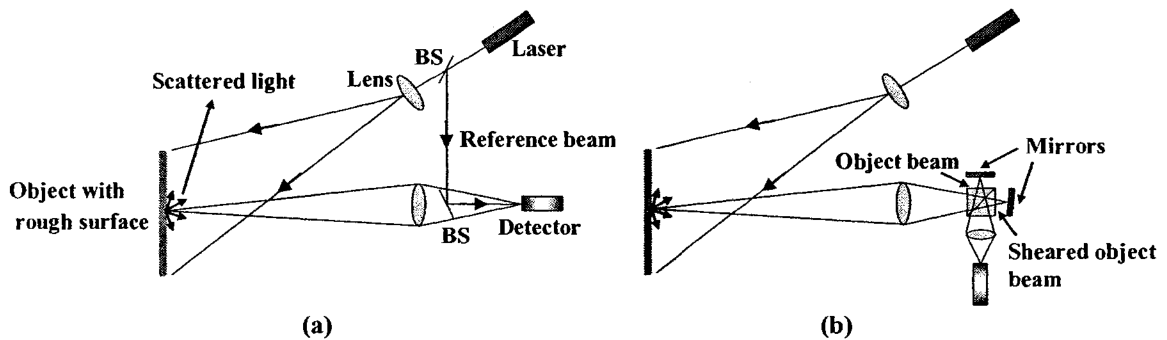

Figure 1.11 Schematic of the speckle interferometry set-ups (a) ESPI and (b) Shearography

1.5 Motivation for Current work

All the techniques overviewed have their own advantages and limitations. One of the main problems of some of these inspection methods is their testing duration which is relatively long. The probe and scanning based methods are such time-consuming methods which are not useful for fast on-line inspection. Another important problem with some of these testing techniques is related to the type of their defect detection system. For example, while imaging the microcracks, regardless of its difficulties, will help to learn

more about their sources and investigate on their behavior, there is not a simple relation between the existence of the microcracks and wafer breakage. It means that even some wafers with microcracks can be processed and transported under moderate loading conditions without any breakage. So, it seems that it is more useful to test the wafers in a way that shows the critical defects which cause the breakage of the wafer under the conditions (stresses) that the wafer will experience in the industrial environment. The critical defects can be detected if the stress distribution in the wafer is almost equal to the real applied stress distribution during the wafer processing and handling. A higher stress distribution will cause the non-serious defects (for example, small cracks) become visible and a lower stress distribution does not allow the critical defects to be observed.

Shearography overcomes these two main disadvantages of the above mentioned inspection methods. One, it is fast since it is a full-field technique. Two, critical defects can be identified as there is a need to apply a specific amount of stress to show the defective areas. Also, shearography has the ability to detect the surface and sub-surface defects simultaneously which can be done only by a few inspection methods such as x-ray, ultrasonic and thermography techniques. Compared to these three techniques, as explained before, shearography has the first priority to be used as an on-line inspection technique due to its shorter inspection time, simplicity and being safer when compared to using x-rays.

1.6 Objective and scope of the research

The objective of this work is to test the feasibility of shearography technique for crack detection in silicon wafers. Though Shearography has been reported in 2004 for identification of sub-surface defects in silicon wafers [27], there is not any work done on the ability of this technique for crack detection in silicon wafers. The scope of this research includes:

- Study the theoretical and practical aspects of the shearography technique for qualitatively evaluation of materials
- Develop a compact and rigid shearography optical set-up
- Perform experiments to optimize the performance of the shearography set-up
- Test the capability of the shearography technique for crack detection in silicon wafers simultaneously with sub-surface defects detection

Chapter 2 Theory of Speckle Interferometry

2.1 Introduction

The speckle interferometric technique was first recognized by Leendertz and Butters in the early 1970s and further research in this field introduced a new area of measuring methods in the world of optical metrology [28]. Electronic speckle pattern interferometry (ESPI) and shearing speckle pattern interferometry (shearography) are the most commonly used speckle interferometry techniques. As explained briefly in previous chapter, in ESPI and shearography, the comparison between the two speckle patterns of the deformed object (before and after deformation) gives the information about the displacement and displacement gradient of the object surface.

Although shearography was at first used for slope measurement [28], Hung developed this method and reported his results for non-destructive testing (NDT) of the materials [29]. As the displacement gradients are the components of strain, shearography can directly provide the strain information of the object deformation. Since the defective areas in materials produce strain concentration areas on the surface, the defects can be simply detected through determination of anomaly areas on the shearography fringe pattern. Because the unexpected movement of the object like its rigid-body motion during the test does not make any strain, shearography is quite insensitive to vibrations and can be used in hostile environments.

Due to simplicity and its insensitivity to vibrations, the application of shearography has been extended in industrial environments for NDT [30-33], strain measurement [34-35] and vibration analysis [36-37]. Based on the need for a qualitative measurement or a quantitative measurement, different type of shearography set-ups can be used.

In this chapter, first the basic theory of the speckle interferometry is explained. Next, the qualitative and quantitative measurements by speckle interferometry techniques are discussed and the fundamental principles of ESPI and shearography are described in detail. Finally the application of shearography in NDE has been reviewed.

2.2 Speckles

When a rough surface is illuminated with coherent light, an observer sees a grainy appearance of the object. The scattered waves from the object surface interfere with each other in space and dark and bright spots will be seen. These spots are called speckles and the whole grainy appearance is named speckle pattern, Figure 2.1. The speckle pattern appears if the wavelength of the illuminating light is smaller than the height variations of the rough surface [22].

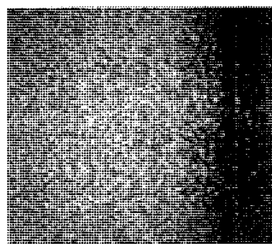

Figure 2.1 Speckle pattern of a rough surface (Al plate) illuminated with laser

The phases of the scattered waves are random due to the different heights of the surface points. These phases are constant in time but vary point to point. So, when the waves interfere with each other, they develop a stationary speckle pattern. Each speckle in the speckle pattern has the phase information of the interference of the scattered waves coming from the related point on the object surface.

Figure 2.2 shows that the speckles can be observed in two ways [38]. When they are seen directly in the space in front of the rough surface, they are called objective speckles, Figure 2.2(a). If an image is taken from the surface of the object, the speckles can be seen in the image, too. In this case, that is most common in speckle interferometry, they are called subjective speckles, Figure 2.2(b).

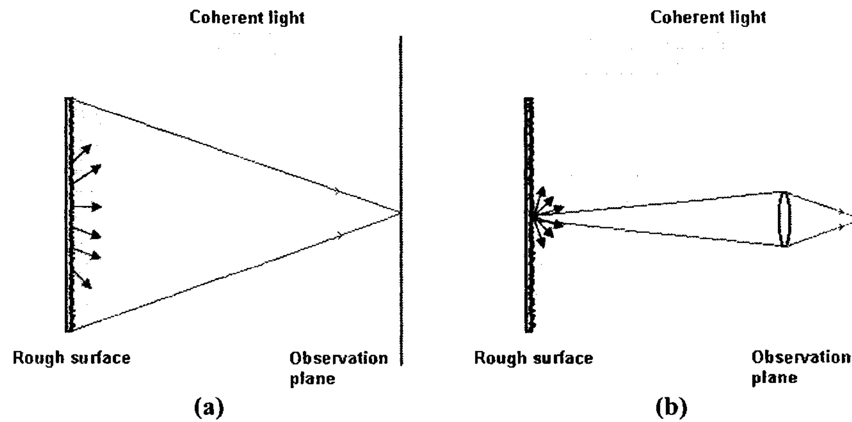

Figure 2.2 Speckle configurations: (a) Objective speckle and (b) Subjective speckle

Assuming a monochromatic polarized and fully developed speckle field, it can be shown that the objective speckle diameter d_s is equal to [25]:

$$d_s = 1.22\frac{\lambda z}{D} \tag{2.1}$$

Where λ is the wavelength of the illumination light, z is the distance between the observation plane and the object surface, and D is the diameter of the illuminated area. Since imaging system is usually used for metrology purpose, the results of the objective speckle field should also be validated for subjective speckle field. For a lens with a focal length of f and a magnification of M and aperture NA, z (the distance between the image plane and the object surface) is equal to f(1+M). For small observation angles, the numerical aperture NA of a lens is equal to $D/2f$. So, in this case, the speckle size can be written as:

$$d_s = 0.61 \frac{\lambda(1+M)}{NA} \tag{2.2}$$

As it can be seen in Equation (2.2), the size of the subjective speckles is dependent on the numerical aperture of the lens in imaging system. The speckles become larger if the aperture of the lens is decreased and vice versa.

In many measurement applications, the speckles are considered as noise and they decrease the precision and accuracy of the results. However, some applications, such as speckle photography, speckle interferometry and shearography have created new measurement methods, using the speckles effect.

2.3 Speckle interferometry

The speckle interferometry is the interference of two speckle fields, or a speckle field and a constant reference wave. The same principles that exist in wave interference can be applied for the speckle interferometry. Considering the speckle pattern is imaged on

(x,y)-plane (image plane on detector) and omit the time dependent part e^{-iwt} (stationary speckle pattern where w is the frequency), it can be written [39]:

$$E_o(x,y) = A_o e^{i(g_o.r - \phi_o(x,y))} \tag{2.3}$$

$$E_r(x,y) = A_r e^{i(g_r.r - \phi_r(x,y))} \tag{2.4}$$

Where E_o and E_r are the electric fields of the object speckle field and constant reference wave (or second speckle field), respectively. Also, A is the amplitude, g is the propagation vectors and φ is the phase constant. The intensity distribution of the interference pattern can be written as:

$$I(x,y) = I_o(x,y) + I_r(x,y) + 2\sqrt{I_o(x,y)I_r(x,y)}\cos(\phi_o(x,y) - \phi_r(x,y)) \tag{2.5}$$

Where I_0 and I_r are the intensity of the object speckle field and constant reference wave (or second speckle field), respectively. The intensity image can be also shown as [25]:

$$I(x,y) = I_0(x,y) + I_M(x,y)\cos\phi(x,y) \tag{2.6}$$

In which I_0, I_M, and ϕ are referred to the background intensity, the modulation intensity and the phase, respectively.

Unlike the classical interferometry, there are no visible fringes in the interference pattern (interferogram) of the speckle interferometry. As mentioned before, the phases in the speckle field vary point to point and so, their difference $(\phi_o - \phi_r)$ also varies randomly in space. So, the information which could be obtained from a single interferogram in speckle interferometry is not very useful and practical, since its phase map is random. The fringes as it appears in classical interferometry can also be achieved in speckle interferometry, if two speckle fields from two different states of the object (before and

after deformation) are compared and this comparison is called speckle correlation and results in correlation fringes.

2.3.1 Correlation fringes

To create the correlation fringes, the interferogram images are used directly. The interferograms can be added or subtracted, and the result will show the points of equal phase difference in the same way that appear classical fringes. This method is more desirable in qualititative measurements, especially in NDE methods. In non-destructive evaluation of the materials, finding the location and size of the sub-surface defects that appears as anomalies in a correlation fringe pattern has the first priority compared to the quantitative measurements that indicate the displacement or gradient displacement of the object surface.

The intensity I of the interferograms for the two different states of the object can be written as:

$$I_1 = I_o + I_r + 2\sqrt{I_o I_r}\cos\phi \tag{2.7}$$

$$I_2 = I_o + I_r + 2\sqrt{I_o I_r}\cos(\phi + \psi) \tag{2.8}$$

Where I_1 and I_2 are the interference patterns intensity, before and after deformation. The deformation causes the phase difference of ψ as shown in Equation 2.8. For creating correlation fringes, there are three methods: Additive processing, Subtractive processing, and Additive-subtractive processing [40].

Additive processing: In this method, the two interferograms will be added to each other and the addition V_{add} can be shown as:

$$V_{add} = |I_1 + I_2| = 2(I_o + I_r) + 4\sqrt{I_o I_r}\cos(\phi + \psi/2)\cos(\psi/2) \tag{2.9}$$

The result V_{add} is named additive correlation fringe pattern. In additive processing, the addition of interferograms can be done by any analog recording devices. So, the camera which is used to record the speckle patterns can record and add the two consequent interferograms and V_{add} can be seen directly on the monitor. Using the camera itself to add the interferograms has two advantages. First, there is no need to have any extra storage to keep the interferograms. Second, since the camera adds the interferograms at the time of capturing them, the correlation fringes are created very quickly and the effect of ambient noise will be decreased to a large extent on the fringes.

As shown in Equation (2.9), the additive correlation fringe pattern has two terms of intensity $(I_o + I_r)$ which are recorded by the camera, even without having the other beam (reference or object beam). These terms are named self-interference terms. The contrast of the correlation fringes in additive processing is very low because of the existence of these self-interference terms.

This poor visibility is the disadvantage of additive processing, as it causes to lose the information of the correlation fringes when it is focused on small areas of the object. Figure 2.3 (a) shows an additive correlation fringe pattern. The pattern was acquired from a fixed-edge circular plate vibrated at 5 KHz.

Performing a spatial Fourier filtering on the additive correlation fringes will help to eliminate the low-frequency noise of the self-interference terms, while the high-frequency noise remains and the contrast is still low.

Subtractive processing: In this method, the interferograms of the two different states of the object will be subtracted from each other and the subtraction V_{sub} can be written as:

$$V_{sub} = |I_1 - I_2| = \left|4\sqrt{I_o I_r}\sin(\phi + \psi/2)\sin(\psi/2)\right| \tag{2.10}$$

Eq. (2.24) shows that there is no self-interference term in a subtraction correlation fringe pattern, bringing the contrast to unity. As it can be seen in Equation (2.10), when the phase difference ψ is equal to $2k\pi$, where $k = 0,1,2,...$, the second sin factor becomes zero and a dark fringe appears. Also, for $\psi = k\pi$, $k = 1,3,5,...$, the sin factor has its maximum value and a bright fringe pattern such as shown in Figure 2.3 (b) can be seen. The appearance of the speckles on the bright fringes is because of the discontinuity in the amplitude and phase of the speckles. Compared to additive processing, the visibility of the subtractive fringes is much better. For qualititative measurements using speckle interferometry, especially NDT applications, the subtraction method is the common method to process the interferograms.

Unlike the additive processing, the subtraction processing method can not be carried out by the camera itself. After capturing each interferogram, it must be digitized and stored. Then, by using a digital image processor, the two interferograms can be subtracted from each other. The disadvantages of this method (compare to the additive processing) are its

additional cost because of the digital image processor, and the results affected by ambient noise due to longer processing time.

Additive-subtractive processing: This method is a combination of both additive and subtractive processing. First, an additive fringe pattern $V_{add.1}$ of the two different states of the object is obtained, using an analog recording device. Then, a phase shift will be applied intentionally on the recording process, and the second additive fringe pattern $V_{add.2}$ will be acquired exactly for the same states of the object that used for the first additive fringe pattern. These additive fringes can be shown as:

$$V_{add.1} = 2(I_o + I_r) + 4\sqrt{I_o I_r}\cos(\phi + \psi/2)\cos(\psi/2) \tag{2.11}$$

$$V_{add.2} = 2(I_o + I_r) + 4\sqrt{I_o I_r}\cos(\phi + \delta + \psi/2)\cos(\psi/2) \tag{2.12}$$

Where δ is the phase shift (usually equal to π) during the acquisition of the second additive fringe pattern. The additive-subtractive fringe pattern will be achieved by digitally subtracting the additive fringe patterns and it can be written as:

$$V_{add-sub} = |V_{add.1} - V_{add.2}| = |8\sqrt{I_o I_r}\sin(\phi + \delta/2 + \psi/2)\sin(\delta/2)\cos(\psi/2)| \tag{2.13}$$

Figure 2.3 (c) shows the additive-subtractive correlation fringe pattern of the same plate shown in figure 2.3 (a) and 2.3 (b). This type of processing has the advantages of both previous methods. The resulting correlation fringe has the contrast of unity (from subtractive processing) and it is not affected by the ambient noise that much of in the subtractive processing (from additive processing), but a complex experimental system to provide phase shift is required.

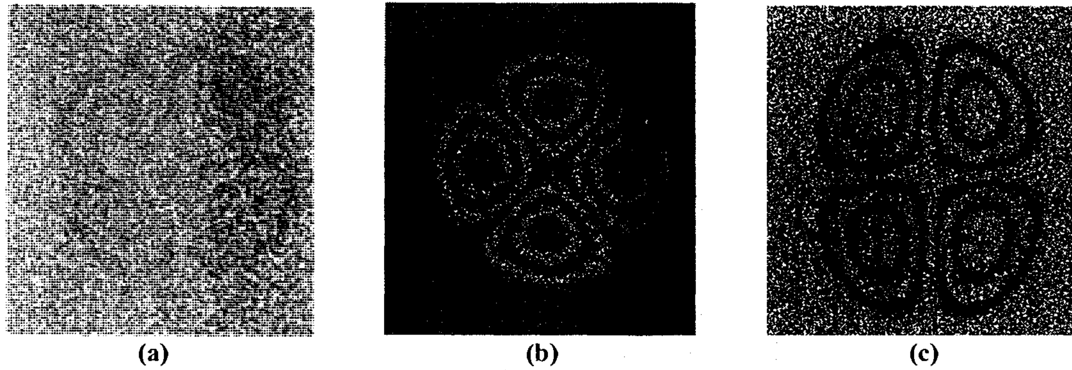

Figure 2.3 Correlation fringe patterns obtained by (a) Additive processing,(b) Subtractive processing and (c) Additive-subtractive processing [40]

2.3.2 Quantitative analysis of the interferograms

The first result of a quantitative analysis of a fringe pattern is a phase map that is related to the intensity distribution of the fringe. Then, the parameter which causes the phase differences at the surface points of the object, which is surface displacement, can be obtained from the phase map. For creating the phase map, the phase difference in each point must be extracted from the fringe pattern. There two group of methods that are used to provide the phase map: Phase shifting methods [41-42] and Intensity based methods [43-46].

Fringe tracking and Fourier transform are the common techniques used in the intensity based methods. The most important advantage of intensity based methods over phase shifting methods is their simplicity that makes them preferred in many industrial applications. Fourier transform technique has been used in this work for processing the fringe patterns and it will be explained in chapter 3.

2.4 Speckle interferometry techniques

The concept of speckle interferometry is used in two different optical set-ups: Electronic speckle pattern interferometry (ESPI) and Shearing speckle interferometry (Shearography)

2.4.1 Electronic speckle pattern interferometry (ESPI)

As its name shows, ESPI is the electronic recording and processing of the speckle interference patterns. The interferograms are captured by CCD camera and either intensity based or phase shifting methods (based on the application) can be used to process the interferograms and extracting the phase map. Figure 2.4 shows the two ESPI optical set-ups.

When speckle pattern interferometry is used to find out the surface displacement, the relation between the phase value $\Delta\phi$ and displacement components can be written as [25]:

$$\Delta\phi(x,y)=\frac{4\pi}{\lambda}w(x,y) \qquad \text{Out-of-plane displacement} \qquad (2.14)$$

$$\Delta\phi(x,y)=\frac{4\pi}{\lambda}u(x,y)\sin\alpha \qquad \text{In-plane displacement} \qquad (2.15)$$

Where $u(x,y)$ and $w(x,y)$ are the displacements components in x and z directions, respectively, and α is the angle of illumination in x-z plane (assuming normal illumination for out-of-plane displacement, $\alpha=0$). The sensitivity of the out-of-plane

displacement measurement is $\lambda/2$ and the sensitivity of the in-plane displacement measurement is $\lambda/2\sin\alpha$.

As shown in Figure 2.4, the reference beam and object beam in an ESPI set-up have different optical path. So, they can be affected differently by noises such as air turbulence, unintentional vibrations and the object rigid body motion, hence it is not suitable for industrial application.

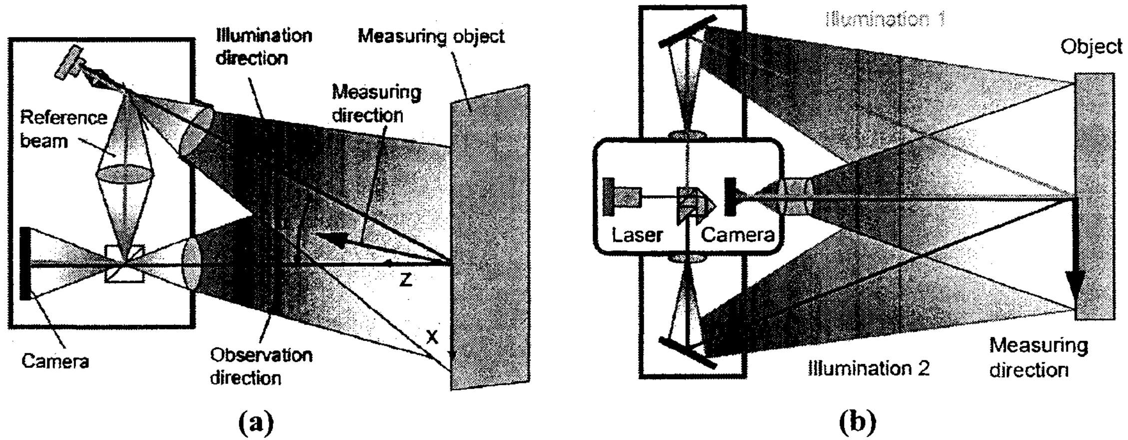

Figure 2.4 ESPI optical set-ups: (a) Out-of-plane displacement measurement and (b) In-plane displacement measurement [47]

2.4.2 Shearing speckle interferometry (Shearography)

To counter the effect of sensitivity to external noise in speckle interferometry shearography is used [26]. If a sheared copy of the object beam is used as the reference beam, the shearography optical set-up, where both the interfering beams have the object beam optical path, can be achieved. The sheared copy of the object beam can be created in different ways. Lateral, radial, rotational and reversal shearing are the different types of the techniques which are used to shear the object beam.

Among these shearing methods, lateral shearing is most commonly used in shearing speckle interferometry (shearography). In this technique the object beam is shifted laterally by a small amount and the interference occurs between the object beam and its shifted copy. For the planar wavefront, the lateral shearing can be obtained by shifting the wavefront in its own plane (either vertically or horizontally) and for the spherical wavefront, the lateral shearing can be obtained by rotating the wavefront about the axis passing through the centre of the curvature of the spherical wavefront.

There are different ways for applying lateral shear on the object beam. The most common ways are: using a shear wedge or a Michelson interferometer. Figure 2.5 shows a shearography optical set-up, which is a Michelson-type shearing speckle interferometer. Besides its simplicity compared to shear wedge, the Michelson configuration also allows the fringe evaluation to be done by phase shifting method [48].

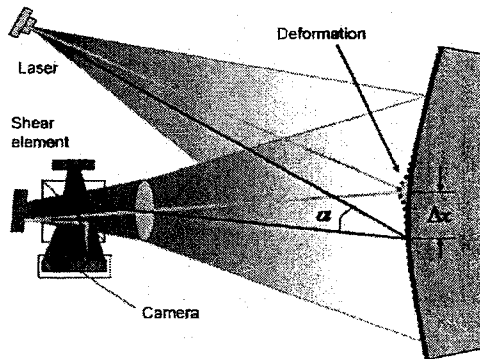

Figure 2.5 A Michelson-type shearing speckle interferometer [47]

The processing techniques of the interferograms in shearography are the same as that explained for speckle interferometry. The phase value in shearography is related to the gradient of the displacement [25]:

For out-of-plane gradient of displacement (illumination in x-z plane):

When shearing is in x-direction:

$$\Delta\phi_x(x,y)=\frac{2\pi\delta x}{\lambda}\left[\frac{\partial u}{\partial x}(x,y)\sin\alpha+\frac{\partial w}{\partial x}(x,y)(1+\cos\alpha)\right] \tag{2.16}$$

When shearing is in y-direction:

$$\Delta\phi_y(x,y)=\frac{2\pi\delta y}{\lambda}\left[\frac{\partial u}{\partial y}(x,y)\sin\alpha+\frac{\partial w}{\partial y}(x,y)(1+\cos\alpha)\right] \tag{2.17}$$

For in-plane gradient of displacement (illumination in x-z plane):

$$\Delta\phi_x(x,y)=\frac{4\pi\delta x}{\lambda}\frac{\partial u}{\partial x}(x,y)\sin\alpha \tag{2.18}$$

$$\Delta\phi_y(x,y)=\frac{4\pi\delta y}{\lambda}\frac{\partial u}{\partial y}(x,y)\sin\alpha \tag{2.19}$$

Where $\frac{\partial u}{\partial x}(x,y)$, $\frac{\partial u}{\partial y}(x,y)$, $\frac{\partial w}{\partial x}(x,y)$ and $\frac{\partial w}{\partial y}(x,y)$ are the in-plane and out-of-plane displacements gradient components, respectively. Also, δx and δy are the shearing amounts in x and y direction, respectively. The sensitivity of the out-of-plane displacement gradient measurement (considering a normal illumination, $\alpha=0$) is $\lambda/2\delta$ and the sensitivity of the in-plane displacement gradient measurement is $\lambda/2\delta\sin\alpha$, where δ is the shearing amount in x or y direction. So, the sensitivity of the shearography can be changed by adjusting the shearing amount.

2.5 Applications of shearography in NDE

Digital shearography has been developed in many different technical points of view in 1990s [26] and its advantage of being full field, non-contact and fast make it as one the

important NDT techniques in recent years. One of the main NDE applications of shearography is for evaluation of composite materials in aerospace and automotive industry. The use of shearography has also been extended to test the pressure vessels and even biomaterials. Regarding the application of shearography in each of these areas, many researches have been done in order to observe the capability of this method for testing the materials and also prove its better potential compared to the other methods [49-56]. In 1999, Hung reviewed the application of shearography for composite structures [49]. Recently, Růžek *et al.* have compared the visual, ultrasonic C-Scan and shearography methods in their work to evaluate and identify the impact defect in sandwich panels [50]. Among these methods, shearography due to its simplicity and reliability found to be the most appropriate technique for inspection of wing and fuselage outer surface. Xide *et al.* have also combined holography and shearography techniques in order to perform quantitative defect detection in thin-walled pressure vessels [51]. Their results were promising and the size and depth of the cracks and cavities could be estimated accurately. Figure 2.6 shows the shearography images of some defected composite structures reported in these works. Also, Narayanan *et al.* have used shearography for non-destructive testing of phantom tissue surfaces [56]. They have simulated the abnormal growth in body cavities by abnormalities in layers of a sample phantom and as it can be seen in Figure 2.7, the defective area could be detected.

The application of shearography for bulk silicon wafers inspection has been done recently in Singapore University [57]. Ganesha *et al.* have done research in this field and the sub-surface defect detection in silicon wafers by using shearography is emphasized in their

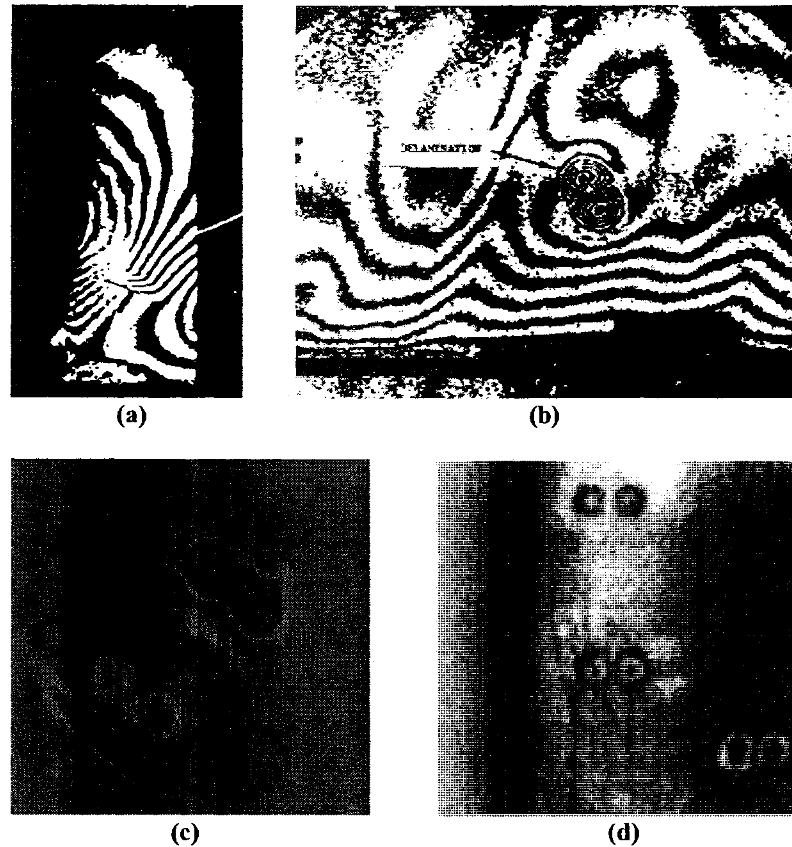

Figure 2.6 (a) a crack in a composite turbine blade stressed by thermal loading [49] (b) a delamination in a filament-wound composite pressure vessel [49] (c) impact damages in a carbon skin sandwich structure stressed by thermal loading [50] and (d) several cavities in a steel 45 pressure vessel [51]

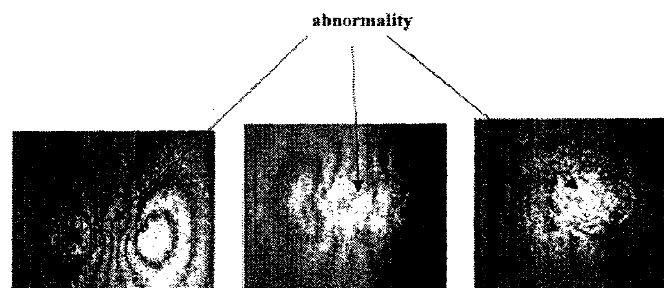

Figure 2.7 Fringe patterns of a phantom specimen with abnormal areas [56]

work [27]. For surface defect detection, they have used SEM and in order to find the defect size and depth, optical profiler has been utilized. Shearography has been used in their work for sub-surface defect detection. By using thermal loading, the positions of the

sub-surface defects were determined due to the anomaly areas on the fringe pattern. However the size of the defects could not be determined perfectly. Figure 2.8 shows the fringe patterns of the sub-surface defects.

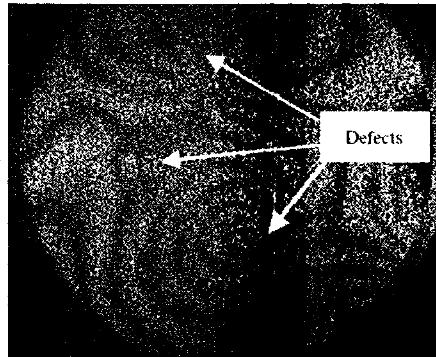

Figure 2.8 Shearography fringe pattern of an unpolished silicon wafer with sub-surface defects [57]

Though Shearography has been used for identification of sub-surface defects in silicon wafers, there is not any work done on the ability of this technique to identify crack and crack propagation. In this work, the ability of shearography for crack detection in silicon wafers at the same time of sub-surface defect detection is investigated.

2.6 Summary

In this chapter, the theory of the speckle interferometry was explained and the ESPI and Shearography methods were described. The application of shearography for NDE in different fields was also reviewed. In the next chapter, the optical arrangement of the shearography set-up and the criteria to choose each component of the set-up is discussed.

Chapter 3 Shearography Optical Set-up

3.1 Introduction

In this chapter the systematic design of the proposed shearography optical set-up is described. In first section, the basic arrangement of the optical set-up is illustrated and in second section, the criteria of selection of each part of the set-up are explained.

3.2 Basic arrangement of the optical set-up

A Diode laser is used to illuminate the sample surface and as it has been shown in Figure 3.1, in front of the output of the laser, a spatial filter is placed to make uniform the light intensity and also a polarizer to adjust the intensity of the light for different surfaces. The spatial filter combined to an objective lens is used to expand the laser light for illuminating the desired testing area. A Michelson interferometer is arranged as the shearing head. A lens with adjustable focus and numerical aperture is mounted on the CCD camera and a bandpass filter is fixed in front of the CCD array. The filter can only pass the wavelengths in the neighborhood of the laser wavelength. So, there is no need to have a dark room and the experiments can be done in the laboratory environment. The mechanical design for applying stress on the silicon wafer surface consists of a fixture and the loading system. The fixture is supposed to clamp all edges of the sample. Two types of loading have been used in the experiments: concentrate force loading and thermal loading. The object is deformed by applying load on its surface and the interferograms are recorded before and after the object deformation. In this work, the

Fringe Processor software is used to process the interferograms and analyze the resulting fringe patterns.

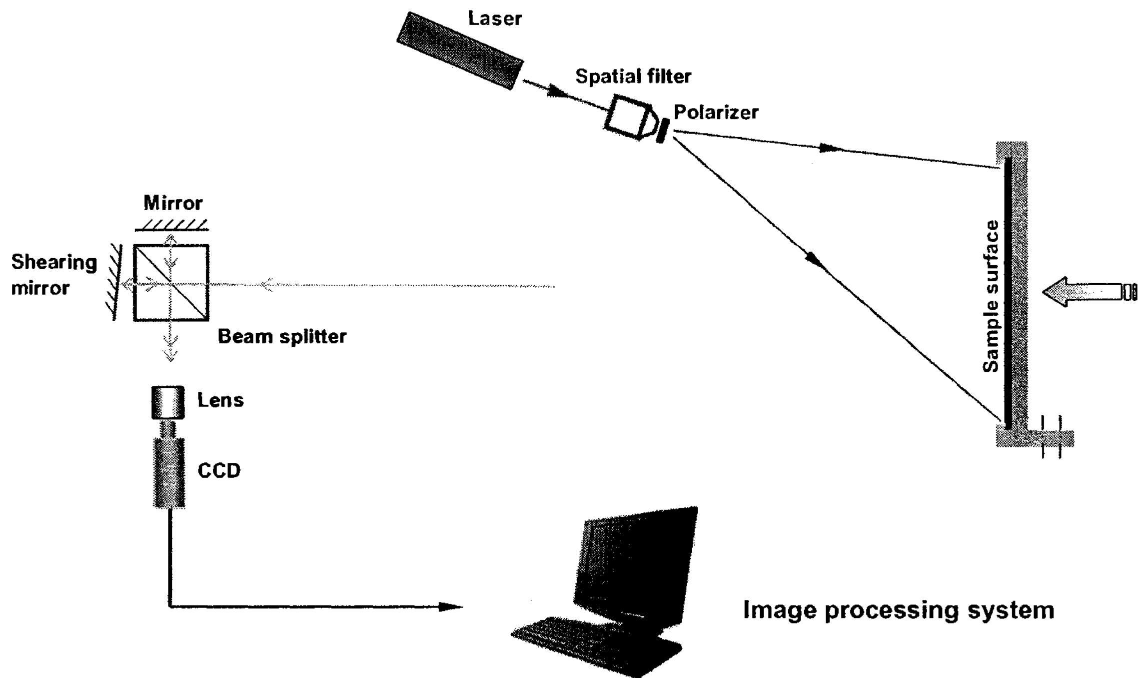

Figure 3.1 The schematic of the shearography optical set-up

3.3 Selection criteria of the optical set-up components

In this section, the components of the Shearography set-up are defined and described. The experimental set-up is arranged on a vibration isolation table and all the components are fixed to the base to relatively avoid the influence of any unwanted vibrations on the optical set-up. As Figure 3.2 shows, the optical set-up is divided to six separately modules. These parts are: the illumination system, the shearing system, the imaging system, the recording system, the image processing system and the mechanical system for

applying load. The characterization of each of these fundamental parts and the criteria to choose the appropriate components for each of them are described in detail in next section.

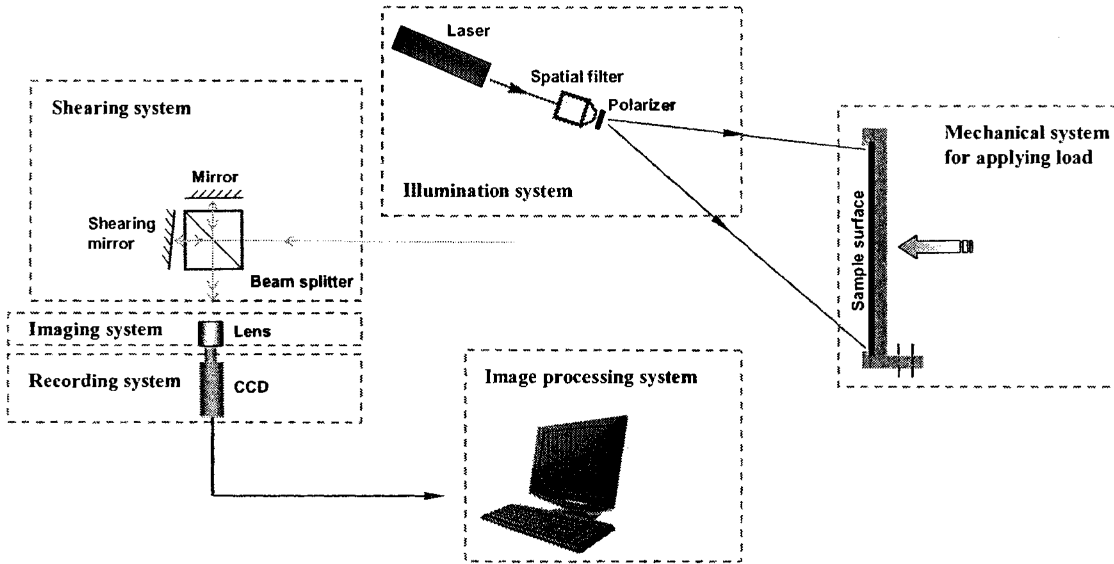

Figure 3.2 The functional components of the shearography optical set-up

3.3.1 The illumination system

Making a small and compact set-up has the advantage of being portable and so, more applicable in different conditions. For this reason, we decided to choose a small laser for the illumination part. Regarding the laser size and its power, the appropriate lasers that can be used for a speckle interferometry set-up have been shown in Table 3.1:

Laser Type	Wavelength	Power		Coherence length
He-Ne laser [58]	633 nm	Up to 50mW	CW	0.2-0.3m
Nd:YAG laser [59]	532 nm	Up to 5W	CW and Pulsed	Many meters
Diode laser [60]	635-980 nm	Up to 100mW	CW and Pulsed	Order of meters
Argon-ion laser [61]	514, 488 nm	Up to 20W	CW	A few centimeters

Table 3.1 Different lasers that can be used for a shearography set-up [25]

Beside the properties of the laser such as its power and wavelength, there is another important factor which should be taken in account in any interferometer. This factor is the laser's coherence length which should be large enough compared to the difference in optical path length between the object beam and reference beam [25]. The building properties of each laser affect its coherence length. Basic components of a laser are: active laser medium (gain medium), pump source which is supposed to apply energy to gain medium and optical cavity in which the laser radiation can circulate between reflectors and pass the gain medium. The laser coherence length is related to the laser optical cavity and the smaller optical cavity causes the smaller coherence length [62].

Moreover, to have the optimal performance of an interferometry set-up, the illumination and recording system should be matched. Considering the sensitivity of the recording device (which is discussed in the recording system section), we should decide about the power and wavelength of the laser.

A Diode Laser is chosen for the set-up because it is simple to use, economical to maintain and do not need much space to sit (they do not have water cooling). The coherent length of the diode lasers with Fabry-Pérot type resonator designs, which are the most common used diode lasers because of their low-cost, can be expected to be short, in the order of a few millimeters at best [25]. Fortunately, in shearography, a large coherence length is not required and it is usually in the order of microns [63]. One of the advantages of shearography over the speckle interferometry is this smaller coherence length due to the absence of the separate reference beam in shearography.

The laser used in this optical set-up is a continuous wave laser and its wavelength and power is 658nm and 65mW, respectively. Due to dust particles and other contaminants in the atmosphere, the laser beam has spatial disturbances. So, a spatial filter must be used in order to filter these disturbances and uniform the laser light intensity. The principle of spatial filtering and its effect on the optical system is shown in Figure 3.3. In the proposed set-up, a 10X objective lens with a 15μm pinhole aperture is used to achieve a uniform laser beam. In front of the output of the spatial filter, a polarizer has been placed in order to adjust the intensity of the light for different surface colors. A precision linear polarizer for visible wavelengths range (430-670 nm) is used in this set-up.

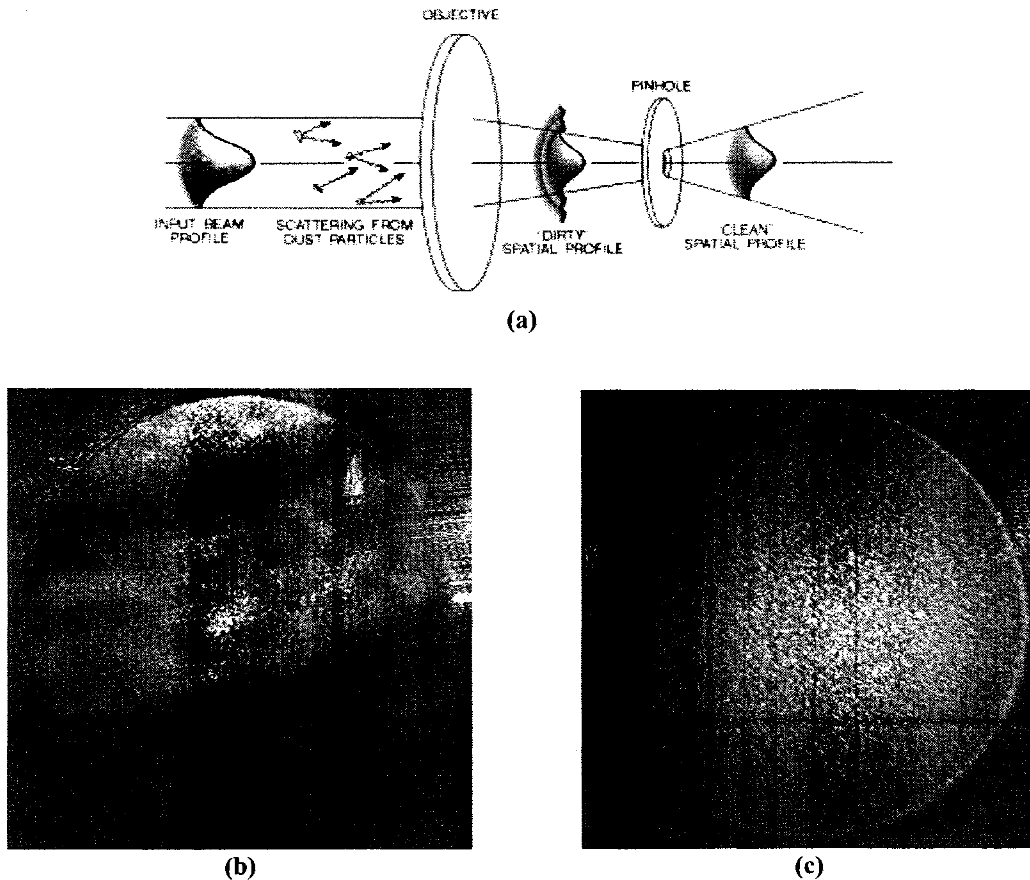

Figure 3.3 (a) Schematic of a spatial filter configuration (b) a speckle pattern before spatial filtering and (c) after spatial filtering

3.3.2 The Shearing system

In shearing speckle interferometry, the object beam interferes with the "sheared" object beam, instead of interfering with reference beam which we have in speckle interferometry.

The most popular way of shearing is lateral shearing, especially in non-destructive testing applications using shearography. For spherical wavefront, as explained before, the lateral shear results from rotating the wavefront about the axis passing through the centre of the curvature of the spherical wavefront, as it has been shown in Figure 3.4 [26].

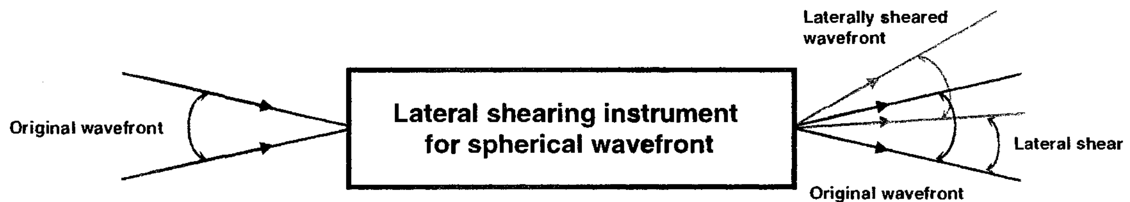

Figure 3.4 Lateral shearing for spherical wavefront

There are different shearing instruments that can be used to apply the lateral shearing, such as a Michelson interferometer, a bi-prism, a wedge or two tilted flat glass plates [26]. The advantage of Michelson interferometer over the other shearing elements is that the amount and direction of the shear can be applied simply by only tilting one of the mirrors positioned on the two sides of the beam splitter.

The shearing instrument in the set-up is a Michelson interferometer. It consists of a cube beam splitter and two flat mirrors, as it has been shown in Figure 3.5. One of the mirrors

is fixed and one of them, which is called shearing mirror, is supposed to rotate around the x (θ_x) and y (θ_y) axes. The scattered light from the object, which passes through the beam splitter, will be divided to two equal beams. The object beam is the one which is reflected from the fixed mirror and the sheared object beam is the one which is reflected from the shearing mirror. The direction of the shearing distance can be defined by choosing the direction of rotation of the shearing mirror, and its magnitude can be adjusted by the amount (degree) of rotation.

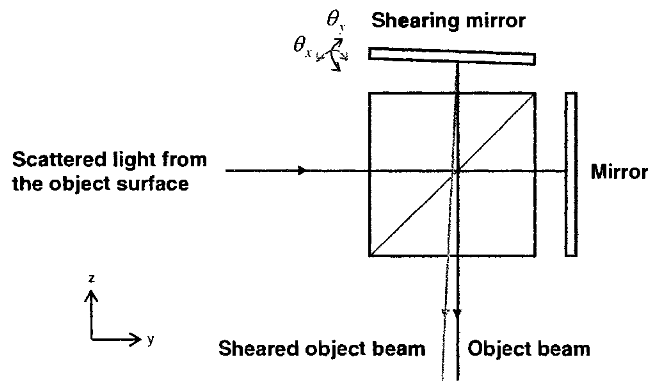

Figure 3.5 The shearing system: Michelson-interferometer

Cube beamsplitters (for visible wavelengths range) are used in this set-up since they have some advantages compare to the plate beamsplitters, such that they are mounted simply and their coating is more slowly degraded, because the beam splitters are sealed in the cube body [64].

To choose appropriate mirrors for an interferometry set-up, some primary parameters such as mirror surface accuracy and its coating should be considered. For the interferometry optical set-ups, where precise images are needed, surface accuracy of

$\lambda/20$ is recommended [64]. However, the flatness of $\lambda/10$ can also be offered, since it is more economical and it can satisfy the desired low beam distortion in a shearography set-up. The most commonly used coatings are metallic coatings because of their good performance and their low price compare to the dielectric coatings. Protected aluminum round flat mirrors with the surface accuracy of $\lambda/10$ are used in the set-up.

3.3.3 The imaging system

The imaging system consists of the lens or lenses that are supposed to transfer the image of the sample to the recording system. Considering the minimum distance needed for placing the shearing head, the object distance (working distance) for the lens(es) arrangement can be found. The dimensions of the inspection area in order to find the required magnification of the lens(es) system is also required. Figure 3.6 shows schematically the working distance and inspection area in the shearography set-up.

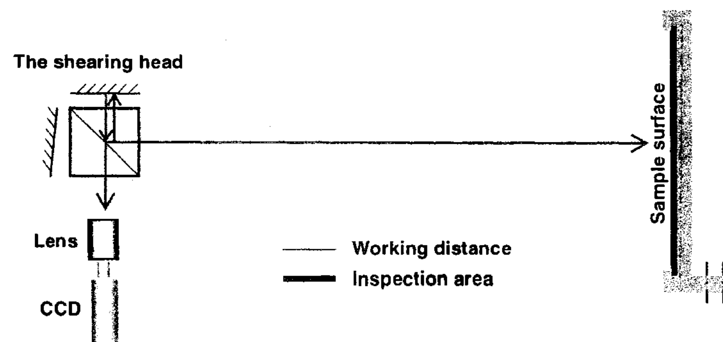

Figure 3.6 Working distance and inspection area shown schematically in the shearography set-up

To have a rigid and more important, a compact optical set-up, we chose to use a fixed focal length lens instead of using a set of lenses. In this way, the optical distortion in the

set-up, which happens more noticeably in the case of utilizing several lenses, has been minimized.

For the imaging system, a Pentax MV lens with adjustable focus and iris is combined with the recording system. This lens has the advantage that the numerical aperture of the imaging system can be adjusted accurately. The working distance in this set-up is 750mm and the inspection area is a 140mm by 100mm rectangular area. The focal length of the imaging lens is 25mm and by using Equation (3.1), the magnification of the system can be obtained [39]:

$$f = \frac{SM}{M+1} \tag{3.1}$$

Where f is the lens focal length, S is the working distance and M is the magnification. Using the mentioned dimensions, M is equal to 0.034. This magnification is applied for CCD imaging plane which is equal to 4.9(h) × 3.7(v) mm.

As discussed before, the numerical aperture is related to the speckle size. The larger the speckle size, the smaller numerical aperture and vice versa. In first section of chapter four, the criteria to choose the optimal speckle size for this shearography set-up will be discussed completely.

3.3.4 The recording system

For recording and processing the speckle patterns, a recording device is needed. The quick response of the recording device is also important, since there is a need to take images consequently in a short period of time (10-20s). The first cameras used in

electronic speckle pattern interferometry were vacuum-tube analogue television cameras, but now the availability, accuracy and linear response of the charge coupled device (CCD cameras) make them as the first choice for detectors in ESPI or shearography. Compare to the camera tubes, CCDs are smaller, more rigid and use less electrical power [65].

The photodetectors in CCD chips contain photosensors in each picture element (pixel) and use silicon as the photosensitive material. Considering the charge transferring methods, there are two types of CCD: frame-transfer CCD and interline-transfer CCD. If the same photosensitive material is used in both of these types of CCDs, frame transfer CCDs give a larger dynamic range and so a better sensitivity. However, frame transfer CCDs are more expensive to fabricate because of their larger chip size and they have lower spatial resolution. But the advantages of interline transfer CCDs are only noticeable when pulsed laser are applied [66].

There is also a parameter named quantum efficiency which is used to show the spectral response of the CCD cameras. Quantum efficiency in standard CCD cameras is around 40% at the wavelength of 700nm [25].

A CV-A11 camera is used in this system. It is mounted on a 3-axis stage and its position can be adjusted for the alignment procedure and inspection of the desired area on the object surface. CV-A11 is a 30 Hz frame transfer camera. The sensing area of CV-A11 is 4.9mm (h) × 3.7mm (v) mm and its cell size is 7.40μm (h) × 7.40μm (v). Table 3.2 shows the specifications and the spectral response of CV-A11.

Specifications	CV-A11
CCD sensor	Monochrome 1/3. IT CCD
Sensing area	4.9 (h) x 3.7 (v) mm
Effective pixels	659 (h) x 494 (v)
Pixels in video output	648(h) x 492 (v)
Cell size	7.4 (h) x 7.4 (v) μm
Resolution horizontal	480 TV lines
Sensitivity on sensor	0.05 Lux, Max gain, 50% video
S/N ratio	>56 dB
Video output (with/without sync.)	Composite VS signal, 1.0 Vpp, 75 Ω Video signal, 0.7 Vpp, 75 Ω
Gamma	o.45 or 1.0
Gain Gain range	Manual - Automatic 0 to +15 dB
Accumulation	Frame

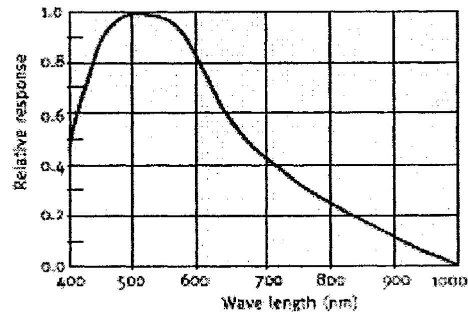

Table 3.2 Specifications and spectral response of CV-A11

There is no need to have a dark room for a shearography set-up [26]. However, the CCD's response to visible light (400-700nm, central wavelength at 550nm) which is higher than for 658nm affects the contrast of fringes in a well lit environment. For this reason, a bandpass filter has been used in front of the CCD camera. This filter only passes the light with the wavelength near the diode laser wavelength (658 nm). This filter allows us to use the shearography set-up in the lab without making any dark condition.

3.3.5 The image processing system

To generate the correlation fringes, there is a need to have the speckle patterns of two different states of the object surface. For this purpose, before and after the desired deformation, the speckle patterns of the object surface are recorded on the CCD camera. The camera is connected to a computer by a trigger cable and the recorded images are transferred to a frame grabber card installed on the computer.

In this optical set-up, the fringe patterns are generated by digital subtraction of these recorded speckle patterns. The experiment has two separate parts: surface slope measurement (quantitative measurement) and defect detection (qualitative measurement). For the quantitative measurement, we need to do the image processing of the resulting fringes, but for qualitative measurement, fringe visualization is adequate to determine the fringe anomaly areas.

To do the image processing of the fringes, Fourier transform method has been used in this system [67]. In this technique, the intensity distribution $I(x,y)$ of the fringe pattern is fitted by a linear combination of harmonic spatial functions. Neglecting the time-dependent parameters, the recorded intensity distribution can be shown by:

$$I(x,y) = a(x,y) + c(x,y) + c^{*}(x,y) \tag{3.2}$$

Where

$$c(x,y) = \frac{1}{2} b(x,y).\exp[i\delta(x,y)]$$

In which $\delta(x,y)$ is the phase difference. In Equation (3.2), the symbol * indicates the complex conjugation. Performing a 2-dimensional Fourier transform on Equation (3.2), we have:

$$I(u,v) = A(u,v) + C(u,v) + C^{*}(u,v) \tag{3.3}$$

Where (u,v) are the spatial frequencies and A, C and C^{*} are the complex Fourier amplitudes. Since $I(u,v)$ is a Hermitean distribution in the spatial frequency domain, its real part is even and its imaginary part is odd. So, the amplitude spectrum $|I(u,v)|$ is symmetric around $I(0,0)$ and as Equation (3.3) shows $A(u,v)$ includes this $I(0,0)$ and

the low frequency components that exist due to the background modulation $I_0(x,y)$. An adapted bandpass filter can be used to remove these undesired disturbances $a(x,y)$ with the mode $C(u,v)$ or $C^*(u,v)$. If for example the mode $C^*(u,v)$ is removed, by performing the inversed Fourier transform on the filtered image, the phase difference value $\delta(x,y)$ can be obtained by:

$$\delta(x,y) = \arctan\frac{\operatorname{Im} c(x,y)}{\operatorname{Re} c(x,y)} \tag{3.4}$$

Considering the sign of the numerator and the denominator, the arctan-function value can be extracted with a period of 2π. This phase map is called saw-tooth-map. To obtain the real phase map, regarding the direction of deformation, a value of 2π is either added or subtracted where the phase jumps from 0 to 2π. This process is named phase unwrapping. The result is a continuous phase map which is achieved after unwrapping the saw-tooth-map. The results of the fringe processing for surface slope measurement of the silicon wafers have been shown completely in chapter 4.

3.3.6 The mechanical system for applying load

The operation of the shearography set-up depends to a great extent on the design of the loading system that is used to deform the object surface. Although shearography is relatively insensitive to vibrations and small rigid body motions (a few microns), it can be affected considerably by the quite large rigid body motions of the tested object. The fringe visibility and its contrast will be decreased due to the speckle pattern decorrelation. If the extent of the speckle decorrelation for two different states of the object becomes greater than the speckle size, no correlation fringes can be generated by the speckle

patterns [68]. For large tested objects and types of loadings which need a long time to deform the object surface, the speckle decorrelation becomes even more critical [26]. To overcome this problem, a fixture that clamps the sample from all its edges was designed. It is also rigidly fixed on the vibration isolation table to avoid any movement during the object deformation.

The common types of loadings used to load the object surface are: concentrate-force loading, acoustic loading, pressure loading and thermal loading. Concentrate-force loading is usually used for the surface slope measurements and numerical evaluation of plane surfaces [26]. In this technique the object is subjected to a central point load and the required displacement in order to get enough number of fringes will be applied by an adequate amount of loading. Acoustic loading is usually used for modal analysis and it can be applied by electromechanical devices such as speakers or piezoelectric transducers [40]. Pressure and thermal loading is usually used for qualitative evaluation of materials. Pressure loading is a slow type of loading and is used to detect defects which are rather far from the object surface. For the structures that are not pressurized during their real operation, a pressure (or vacuum) chamber is needed to surround them either locally or entirely. In thermal loading technique, the object is heated up or cooled down and the temperature gradient will induce deformation on the object surface. Flash lamps or lasers are usually used to apply thermal loading.

In the experiments, concentrate-force loading is used to measure the surface slope of a silicon wafer in order to see the reliability of the arranged out-of-plane displacement

gradient optical set-up. The loading unit is a cylindrical bar with a rounded tip and it is positioned exactly behind the center point of the object surface. The loading unit is connected to a motion controller which can control the movement of the bar in the range of micrometers. For the defect detection in silicon wafers, an infrared lamp is used to apply thermal loading on their surface. A small room was designed for the infrared lamp to avoid the effect of its intensity on the optical set-up.

3.4 Summary

In this chapter, the components of the proposed Shearography set-up were defined and described. For this purpose, the optical set-up was divided to its fundamental parts. The characterization of each of these parts and the criteria to choose the appropriate components for each of them were discussed in detail.

Chapter 4 Results and Discussion

4.1 Introduction

The experiments performed in this research can be categorized into two main groups. The first group has been done to optimize and test out the performance of the optical set-up and the second one has been done to investigate the capability of the system to be used in an industrial environment for inspection of silicon wafers. In this chapter, the more important experiments in each of these groups will be explained. First, the criteria to choose the optimal speckle size, the loading procedure to get fringe pattern and the surface slope measurement to see the reliability of the set-up will be described. Then, the investigation on crack and sub-surface defect detection in silicon wafers will be explained and the results will be discussed.

4.2 Optical set-up optimization

4.2.1 Optimal speckle size

Finding the optimal average speckle size is one of the main parts in arranging any speckle interferometry set-ups. High contrast and low speckle noise fringes can be only obtained by the optimum determination of the speckle size [69]. Many researches have been done to investigate the relation between the speckle size and the spatial resolution of the recording device [69-71]. If the average speckle size is too small compared to the spatial resolution of the recording device, the intensity of each speckle can not be distinguished properly by the image processing software. Choosing the smaller average speckle size

will increase the spatial resolution of the speckle patterns, decrease the noise in the phase map and improve the fringe contrast. However, choosing the larger speckle size will reduce the effect of the decorrelation on the speckle patterns due to the object movement during its deformation.

In this work, as a trade off and observe the resulting fringes visibility, the ratio between the spatial resolution of the CCD camera and the optimum speckle size is found to be 3:1. (CCD cell size: 7.400μm, speckle diameter: 2.490μm). To show the calculation for obtaining the speckle size, as we had in chapter two, the speckle diameter can be obtained by:

$$d_s = 0.61\frac{\lambda(1+M)}{NA}$$

Where in this set-up, λ is 658nm and M is 0.034. The numerical aperture is equal to $1/2F\#$ [64] and the *f*-number $F\#$ can be adjusted on the lens. The $F\#$ in this set-up is 3. So, by calculating the speckle diameter, it becomes equal to 2.490μm.

To have a high contrast fringe pattern, the speckles must be precisely in-focus and have sufficient light intensity. The low-intensity speckle patterns cannot provide accurate data for fringe formation and high-intensity speckle patterns over saturate the middle pixels of the CCD camera and cause to loose the information even in neighboring pixels [65]. Figure 4.1 shows the examples of out-of-focus, low-intensity and optimal speckles in a speckle pattern. The results of subtraction of these speckle patterns from two different states of the object have been shown in Figure 4.2. As it can be seen in Figure 4.2(c),

good quality fringe patterns can be only obtained in the case of formation of optimal speckles.

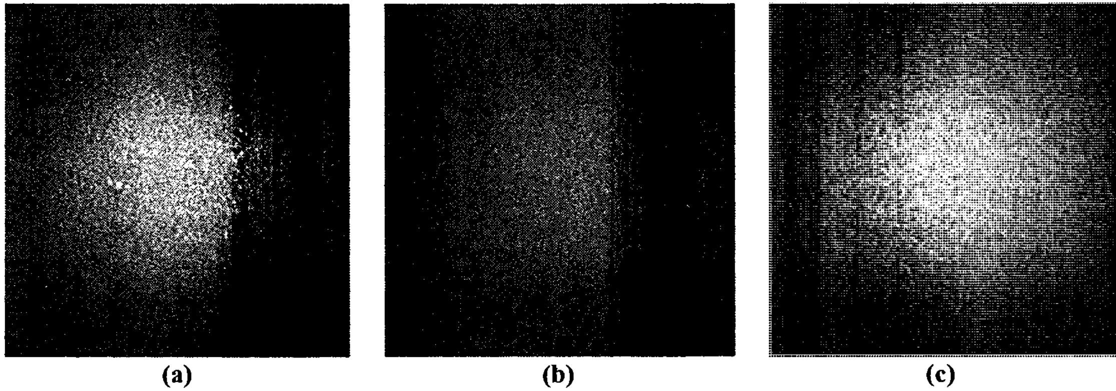

Figure 4.1 (a) Out-of-focus speckles (b) low-intensity speckles and (c) optimal speckles

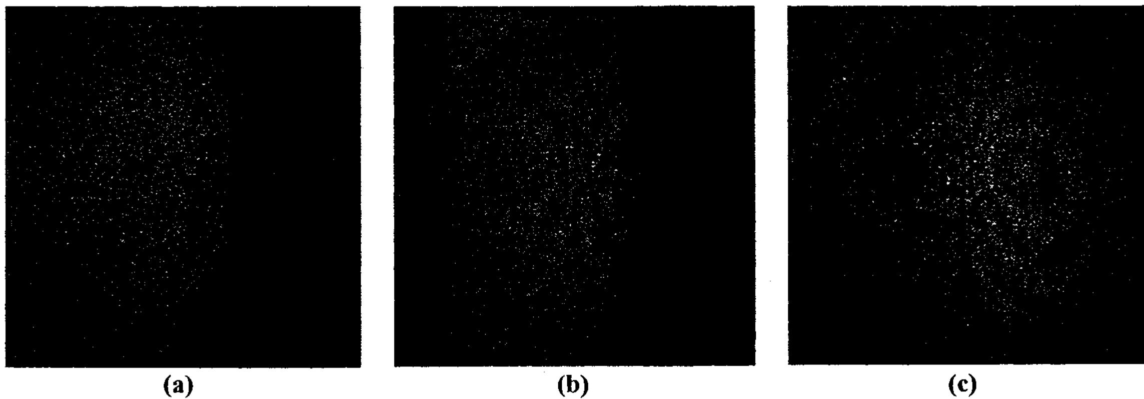

Figure 4.2 Subtraction of (a) Out-of-focus speckle patterns (b) low-intensity speckle patterns and (c) optimal speckle patterns

4.2.2 Correlation fringe formation

To create correlation fringe patterns, several loading trials with different shearing amounts have been performed to find out the required range of displacement of the object for obtaining sufficient number of fringes. In this part of experiments, mechanical loading is applied and as mentioned in previous section, a motion controller is used to measure the center-displacement of the object. Out-of-plane gradient-displacement shearography

set-up is more sensitive to decorrelation compare to the other speckle interferometry set-ups [68]. So, applying the load should be in the way that does not cause a noticeable rigid body motion of object. After applying the load, the images of the deformed object surface are captured after a few seconds delay in order to stabilize the small vibrations that are induced on the object surface by the loading unit.

To perform the trials of getting sufficient fringe orders, a 100mm square Aluminum plate with a thickness of 0.5mm was used in this part of experiment. The surface roughness data of Al plate has been included in Appendix 1. The Al plate was fixed along its edge and the loading unit was positioned exactly behind the center of it. The shearing amount is adjusted for 10 mm to get high order of fringes by a small amount of loading. After several trials, we found the proper range of center-displacement of the Al plate. In each step of loading, we applied 5μm displacement on the center of the plate and recorded the following speckle pattern. By digitally subtracting the resulting speckle patterns, the correlation fringe patterns can be obtained as they have been shown in Figure 4.3. The fringe visibility decreases in high order fringes because of the increasing intensity of the hills in their patterns. The tilt and in-plane displacement of the object surface should also be considered as both of them will gradually decrease the fringe visibility [68]. As observed in experiment and it has been shown in Figure 4.4, the decorrelation happens at 30μm displacement.

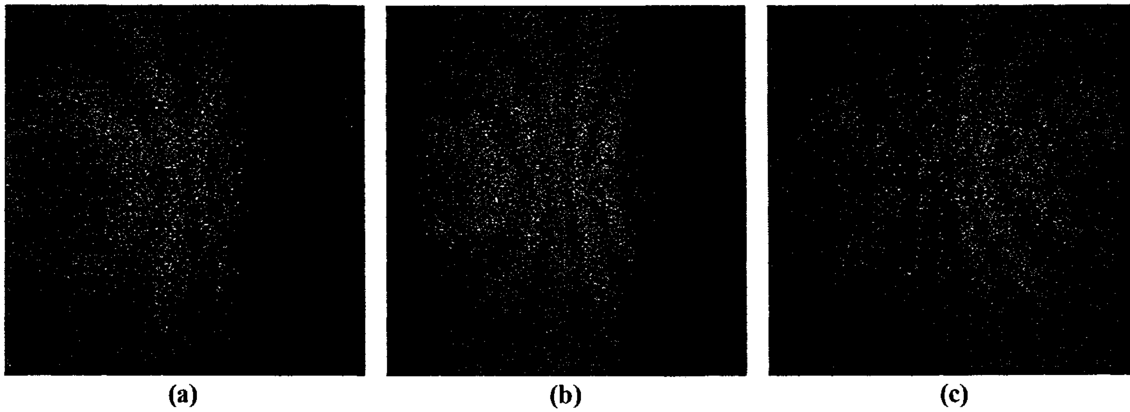
(a) (b) (c)

Figure 4.3 Shearography fringe patterns resulted from subtraction of speckle patterns after (a) 5 μm (b) 10 μm and (c) 15 μm center-displacement of the Al plate

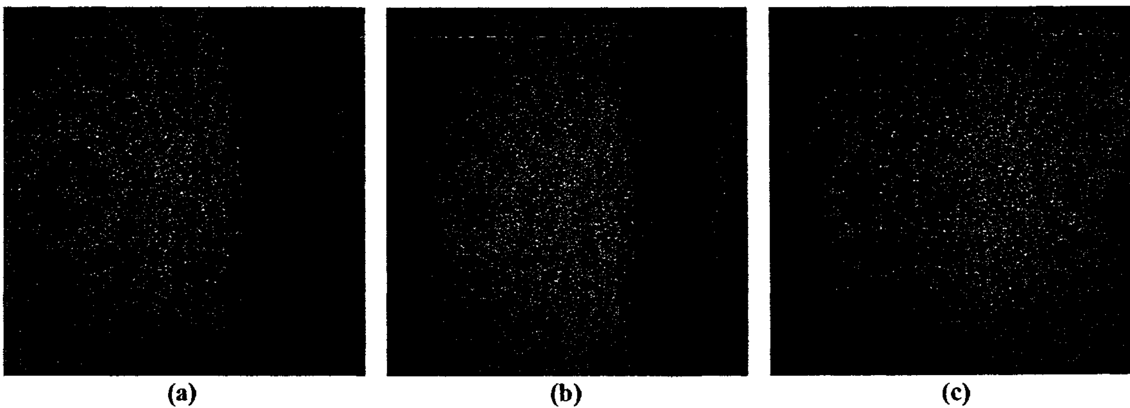
(a) (b) (c)

Figure 4.4 Shearography fringe patterns after (a)20 μm (b) 25 μm and (c) 30 μm center-displacement of the Al plate

To see the capability of the system for different materials, a composite material was also tested. The sample this time was a 100mm square carbon composite plate with a thickness of 1.2mm. Since the composite sample surface was too smooth, its surface was coated with a white powder (spray paint) in order to improve the diffuse reflectivity of the sample surface and reduce its specular reflectivity characteristics [72-74]. The surface roughness data of composite plate has been included in Appendix 1. After several trials, the proper center-displacement of the sample to get visible fringes was found 7μm. The resulting fringe patterns have been shown in Figure 4.5. This time, among the results, the fringe patterns obtained with the shearing amount of 7 mm (smaller than those of Al

fringe patterns) have been illustrated in order to show the consequence of fringe formation with a smaller shearing amount. As shown in Figure 4.5, the decorrelation happens after 42μm displacement.

It was expected that the decorrelation happen around the same distance of Al plate. But, since the carbon composite plate is much stiffer than the Al plate, the loading unit had more backlashes and its inaccuracy affected the results.

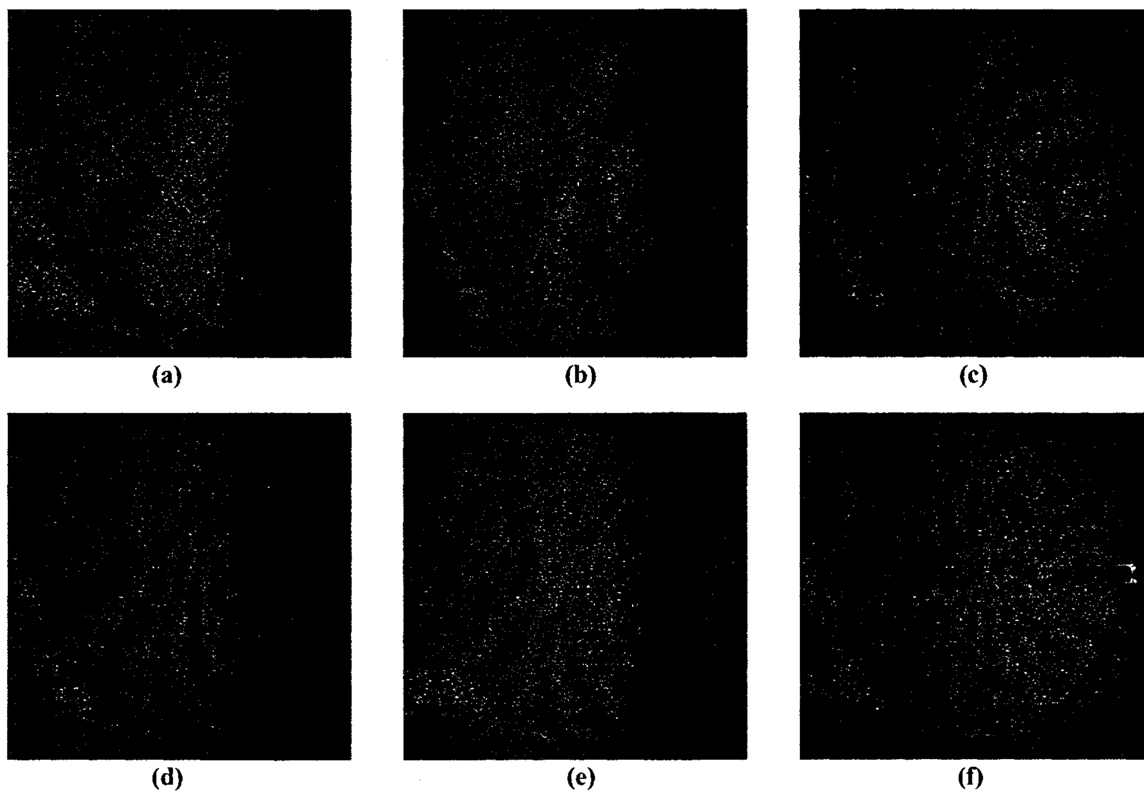

Figure 4.5 Shearography fringe patterns after (a) 7 μm (b) 14 μm (c) 21 μm (d) 28 μm (e) 35 μm and (f) 42 μm center-displacement of the carbon composite plate

The preliminary results of the shearography set-up were promising and it is all set to do the experiments on silicon wafers. In these parts of experiments, in order to increase the accuracy of the system, the set-up has been arranged for an out-of-plane displacement

gradient measurement. The laser illumination, instead of being 30° that it was in previous experiments, is applied almost normal to the sample surface by using a second beam splitter.

4.2.3 Surface slope measurement

In order to increase the fringe visibility and get high order of fringes, the set-up has been arranged for a pure out-of-plane displacement gradient measurement [68]. So, to see the reliability of the fringe patterns, a quantitative analysis of them has been done. For this purpose, we have processed the fringe patterns with Fourier transformation technique and measured the surface slope (out-of-plane displacement gradient) of the object surface and compared the result with the outcome from theory.

As Equations (2.16) and (2.17) show, the out-of-plane displacement gradient of the surface object can be measured if there is a normal illumination ($\alpha = 0°$). Since the term $(1+\cos\alpha)$, appeared in Equations (2.16) and (2.17), will not be zero under any conditions, the in-plane displacement gradient component can not be determined with a single beam shearography set-up. In the case of a normal illumination, the in-plane displacement gradient will be omitted and the out-of-plane displacement can be calculated from the phase data. Figure 4.6 shows schematically the proposed shearography set-up with a normal illumination.

In this re-arranged set-up, the reflection of the laser center point on the first beam splitter appeared as a noise on the interferograms as it has been shown in Figure 4.7. To avoid

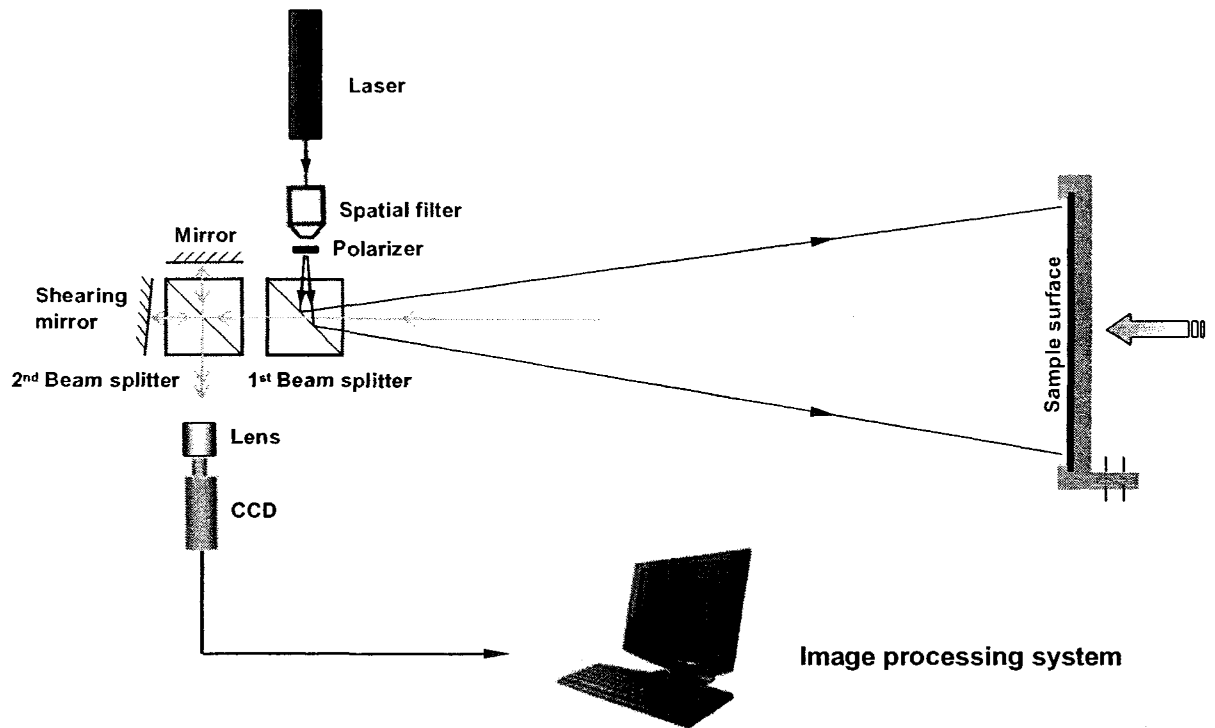

Figure 4.6 Optical arrangement of a shearography set-up for normal-illumination

this, there was a need to have a small illumination angle which could take out the noise out of the fringe patterns. Regarding the fixture window diameter which is 60mm, the optimum movement of 30mm of the noise was predicted. Since the distance between the first beamsplitters and sample was 580mm, an 3° angle of illumination was needed to provide 30mm of movement. The angle of laser illumination was put for 13° and the beam splitter was positioned with a small deviation angle of 5°. As it has been shown in Figure 4.8, the 3° angle of illumination was achieved and the noise spot was put out of interferogram images. Since this angle is smaller than 5°, a normal illumination was assumed for the phase data calculation.

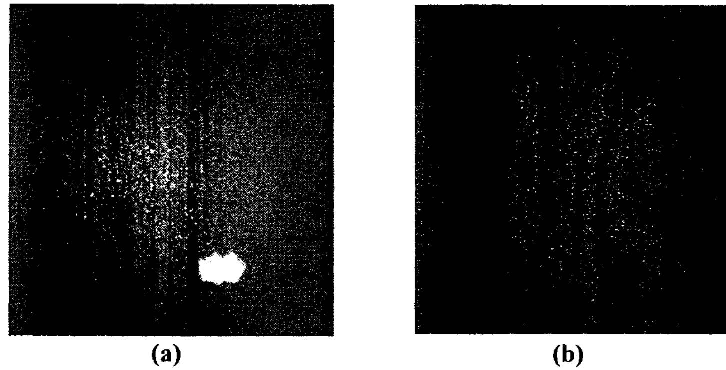

Figure 4.7 (a) Speckle pattern with a noise spot and (b) resulting fringe pattern with loss of information in noise area

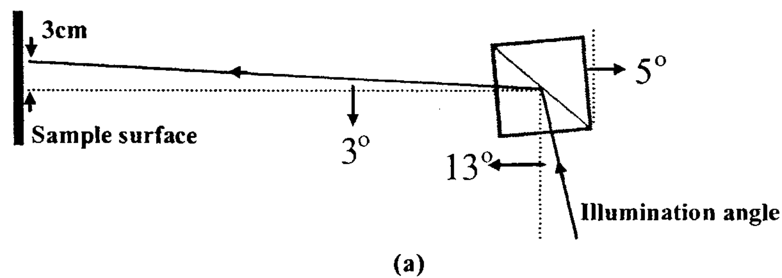

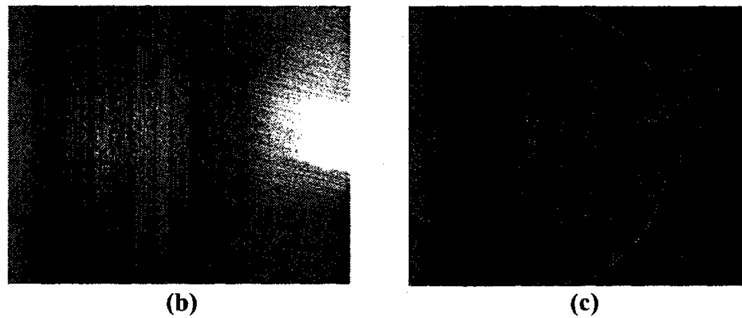

Figure 4.8 (a) Schematic of re-arranged set-up (b) speckle pattern without noise spot inside and (c) fringe pattern without any area of loss of information

The sample in this part of experiment is a 100mm diameter silicon wafer with a thickness of 500μm. Figure 4.9 shows the surface roughness of the sides of the silicon wafer obtained by an optical profilometer. As it can be seen, there is a comparable difference between the roughnesses of the sides of the silicon wafers. As mentioned in section 2.2, the wavelength of the laser must be smaller than the height variations of the rough surface in order to obtain a speckle pattern. Since the wavelength of the laser in this

experiment is 658nm, the unpolished surface of the wafer can only be used in the experiments. The surface roughness data of wafer has been included in Appendix 1

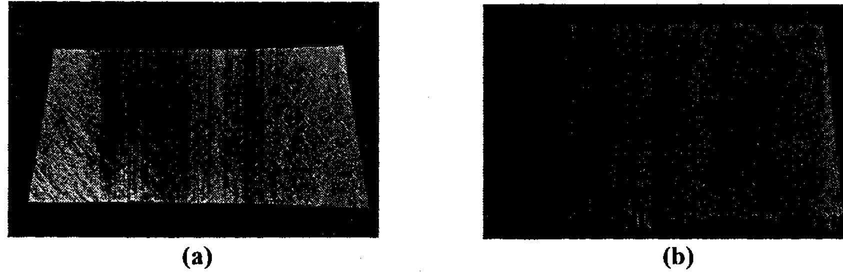

Figure 4.9 Silicon wafer surface roughness (a) back side (polished side) Ra: 5.89nm and (b) front side (unpolished side) Ra: 686.52

It is clamped along its edge and its center is displaced with the step of 2μm. Figure 4.10 shows the resulting fringe patterns. The shearing amount is adjusted for 9mm.

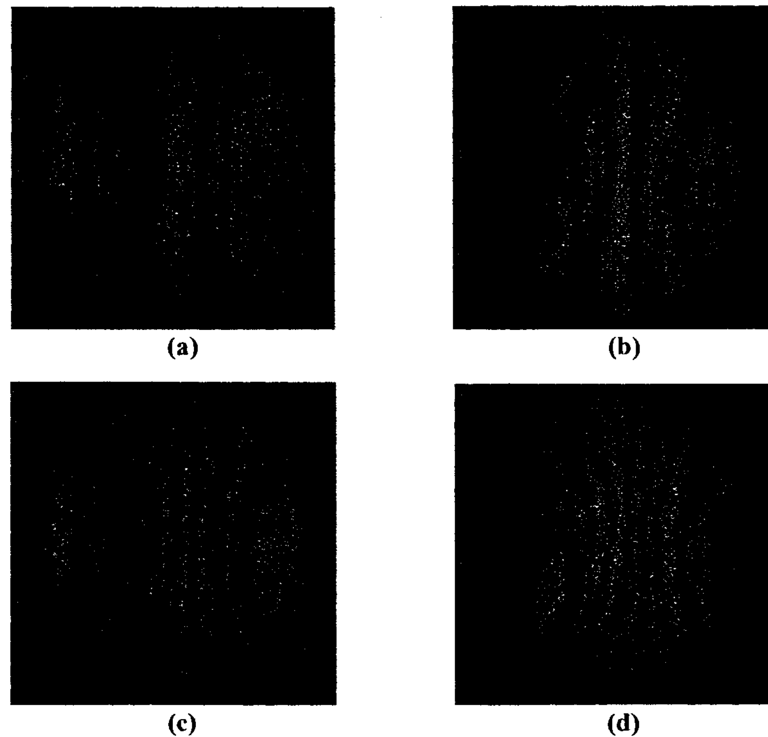

Figure 4.10 Shearography fringe patterns (from a normal illumination set-up) after (a) 2μm (b) 4μm (c) 6μm and (d) 8μm center-displacement of the silicon wafer

To have a good fringe processing procedure, the number of fringes must be large enough in order to separate the spectral orders to allow filtering at the spatial frequency of the fringes [75]. The fringe pattern (c) has been chosen from Figure 4.10 for Fourier transform fringe processing, as explained in chapter 3. After creating the fringe pattern, electronic noise filtering is used to improve the fringe visibility. Figure 4.11 shows the fringe pattern before and after the electronic noise filtering.

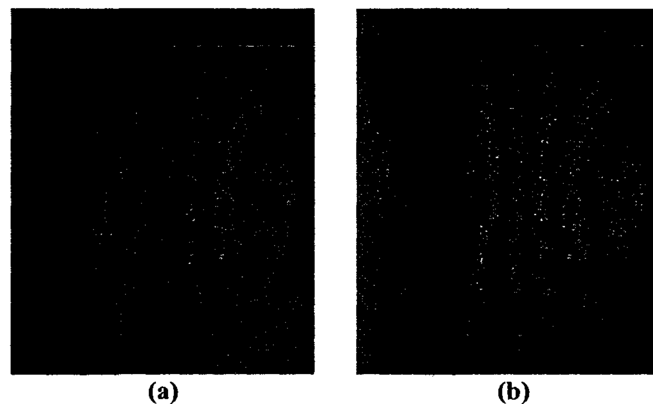

Figure 4.11 Shearography fringe pattern (a) before performing electronic noise filtering and (b) after performing electronic noise filtering

Fourier transformation is performed on the filtered fringe pattern as explained in chapter 3. Before unwrapping the phase map, there is a need to perform interpolation on the resulting phase map because of the high level of discontinuity around the fringe pattern area. The Fourier transformation has been done on an area of 256 by 256 pixels (appropriate 2^n pixel size regarding the fringe size for performing Fourier transformation) and in order to remove the discontinuities, an area of 165 by 210 pixels has been interpolated. The interpolated phase map was unwrapped and low pass filtered in order to remove the high frequency noises. For Fourier transformation technique, since the sign of deformation cannot be obtained from fringe analysis, knowing the direction of

deformation is necessary. Since the phase difference is only of interest in shearography, in order to compare the experimental and theoretical results in this work, based on the direction of deformation in the experiment, the inflection line of the phase map is shifted to the center line of the sample through adding the average of maximum and minimum phase value. Figure 4.12 shows the 3-D plot of phase variation of deformed silicon wafer obtained by Fourier transformation and Figure 4.13 shows the resulting phase map, interpolated phase map and unwrapped phase map on the central cross section of the wafer.

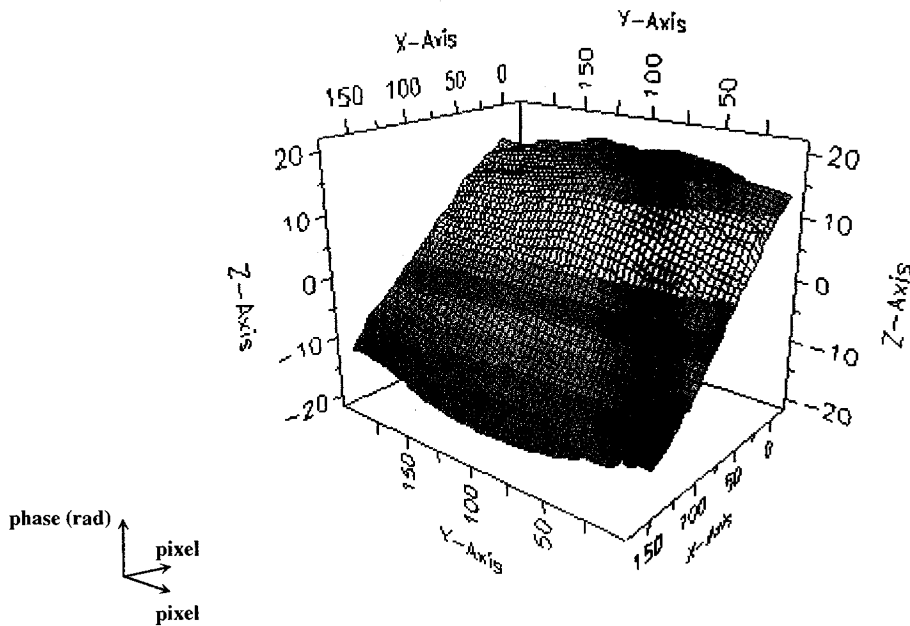

Figure 4.12 3-D plot of phase variation of the deformed silicon wafer (center-displacement of 6μm) obtained by Fourier transformation low pass filtered unwrapped phase map with zones shown between fringes in the unwrapped phase map

As it can be observed in Figure 4.12 (a), the fringe pattern has a small angle with the horizontal line. This rotation appeared due to the off-center applied concentrate force on the silicon wafer. Because of the high stiffness of the silicon wafer, the sensitive loading unit deviates from its straight direction during the test.

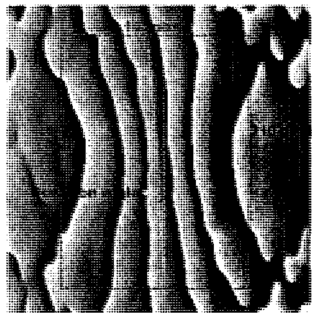

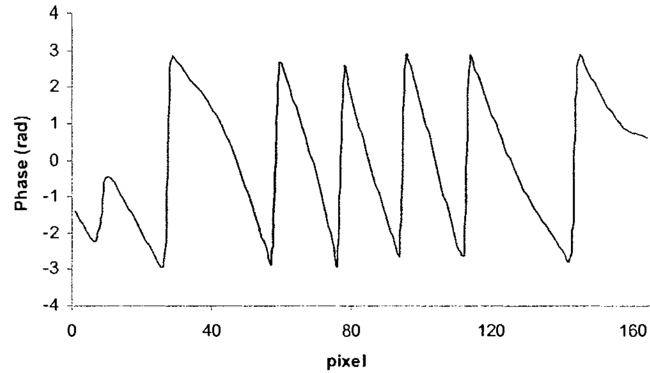

(a)

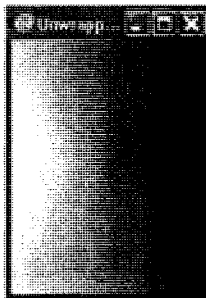

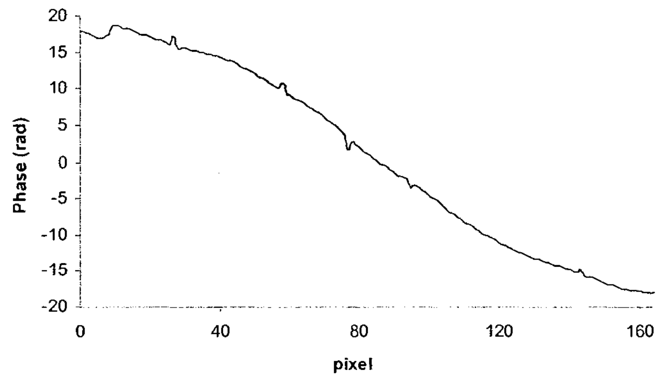

(b)

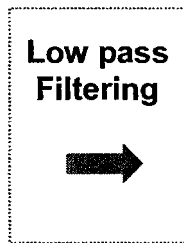

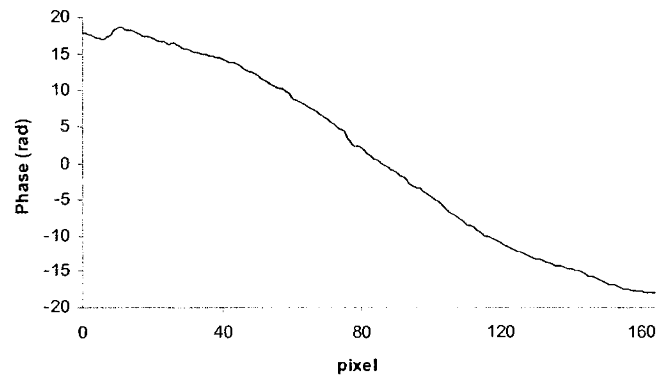

(c)

Figure 4.13 Phase variation on central cross-section of the deformed silicon wafer (center-displacement of 6μm) obtained by Fourier transformation (a) interpolated wrapped phase map (b) unwrapped phase map and (c) low pass filtered unwrapped phase map

Since the shearing amount is adjusted in x-direction, the out-of-plane displacement gradient of the surface can be obtained by using equation (2.16) if a normal illumination ($\alpha = 0°$) is considered. By placing the value of λ (658 nm) and δ (9 mm) in equation

(2.18), the out-of-plane gradient displacement can be obtained from the phase map in Figure 4.13 (c) and it has been shown in Figure 4.14:

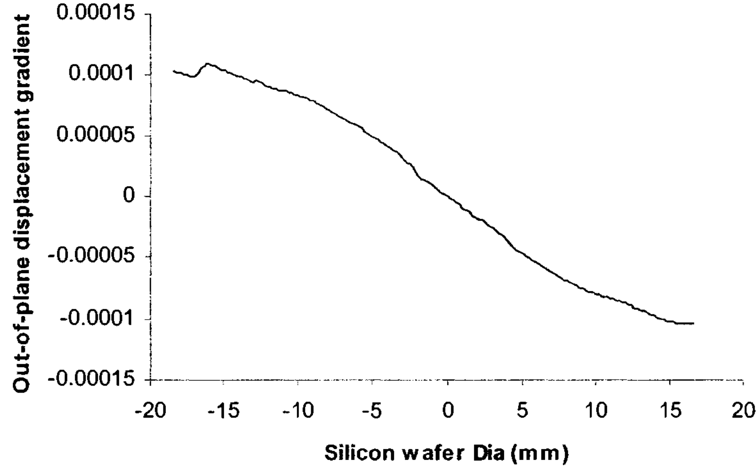

Figure 4.14 Out-of-plane displacement gradient of the center cross section of the silicon wafer obtained from low pass-filtered unwrapped phase map

For comparison with theoretical model, we have calculated the out-of-plane displacement gradient of a fixed edge circular plate with a thickness of 500μm and diameter of 100mm which is loaded by central concentrated force [76]. As the same in the experiment, the center-displacement of 6μm is assumed for the circular plate. Equation 4.1 shows the theoretical relation between the out-of-plane displacement gradient and center displacement of the circular plate along its center line (y=0):

$$\left.\frac{\partial w}{\partial x}\right|_{y=0} = \frac{4w_{\max}}{a^2} x \ln(x) \tag{4.1}$$

Considering wafer surface is imaged on the (x-y) plane, $\frac{\partial w}{\partial x}$ is the out-of-plane displacement gradient, $w_{\max}$ is the center displacement and a is the circular plate radius.

The comparison between the theoretical and experimental results has been shown in Figure 4.15.

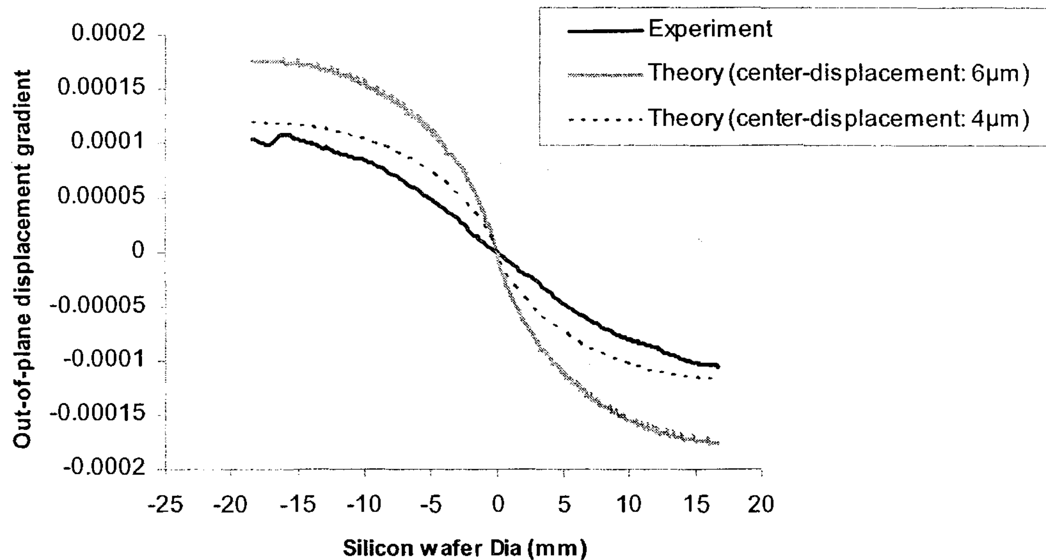

Figure 4.15 Comparison between the theoretical out-of-plane displacement gradient of the silicon wafer and the shearography result

As mentioned before, the applied force on the center of the wafer was not exactly perpendicular to the plane of the wafer and so, an accurate amount of 6μm displacement on the wafer can not be assumed. As the theory graph of the 4μm displacement shows in Figure 4.15, the center displacement of the wafer is closer to 4μm and it shows that the displacement of the wafer center was definitely smaller than 6μm. A part of the difference between the theory and experimental result can also be attributed to the backlash in the loading unit. In-plane-displacement gradient, which had been omitted it in equation (2.16), also plays a role in the difference between the theory and experimental result. As explained before, the illumination angle was 3°. The rest of the difference between theory and experimental results can be because of the Fourier transformation errors that appear due to the low visibility of the fringe patterns.

4.3 Non-destructive evaluation of silicon wafers

As discussed in chapter one, the stability of silicon wafers is one of the main parameters which should be take in account for generating the new type of thin wafers and solar cells. Since the defects in silicon wafers, reduce considerably this stability during loading the wafers in their producing or transporting process, there is an inevitable need to have an inspection system for defect detection in wafers in order to determine the unstable ones. In this research, shearography has been used to detect some types of most common faults in thin silicon wafers. By using thermal loading, the cracks and sub-surface defects in silicon wafers have been identified. The impracticality of using concentrate force loading for defect detection in silicon wafers have been also investigated and discussed.

4.3.1 Crack detection on silicon wafers

Cracks are more probable to be appeared at the edges or on the surface of the silicon wafers due to the sawing or laser cutting. Since the edge cutting is made by an inside-diameter (ID) saw, while surface cutting is made by a wire saw, the edge cracks have usually larger size than surface cracks and so they are more serious [77-79]. Wafer breakage will happen due to the extra stress applied in a way that causes growing the cracks or increasing the residual stress higher than the critical stress. By applying certain stress on the silicon wafers, the critical cracks (and defects) can be distinguished as strain concentration areas on the shearography fringe patterns and the useless wafers can be rejected before entering the production line.

A stress distribution can be created in the silicon wafer by applying a temperature gradient on its surface. In the experiment, an infrared lamp is used to generate a thermal stress in the wafer through optical heating. The amount of applied thermal stress can be controlled by the light intensity and the time of illumination.

Methodology of image capturing: In this work, the fringes are created through cooling down the wafers. The cooling down procedure of the wafer is slower compared to heating up the wafer. So, there is several seconds more to record the speckle patterns. The wafers were heated up to 55°C (90seconds) and the fringe patterns were generated from the images captured in 3 second intervals while cooling down. For example, the second fringe pattern is created by subtraction of the speckle pattern imaged at starting the cooling down and the speckle pattern imaged after 6 seconds (during cooling down the wafer). The inspected perfect wafers with this method have been shown in Figure 4.16.

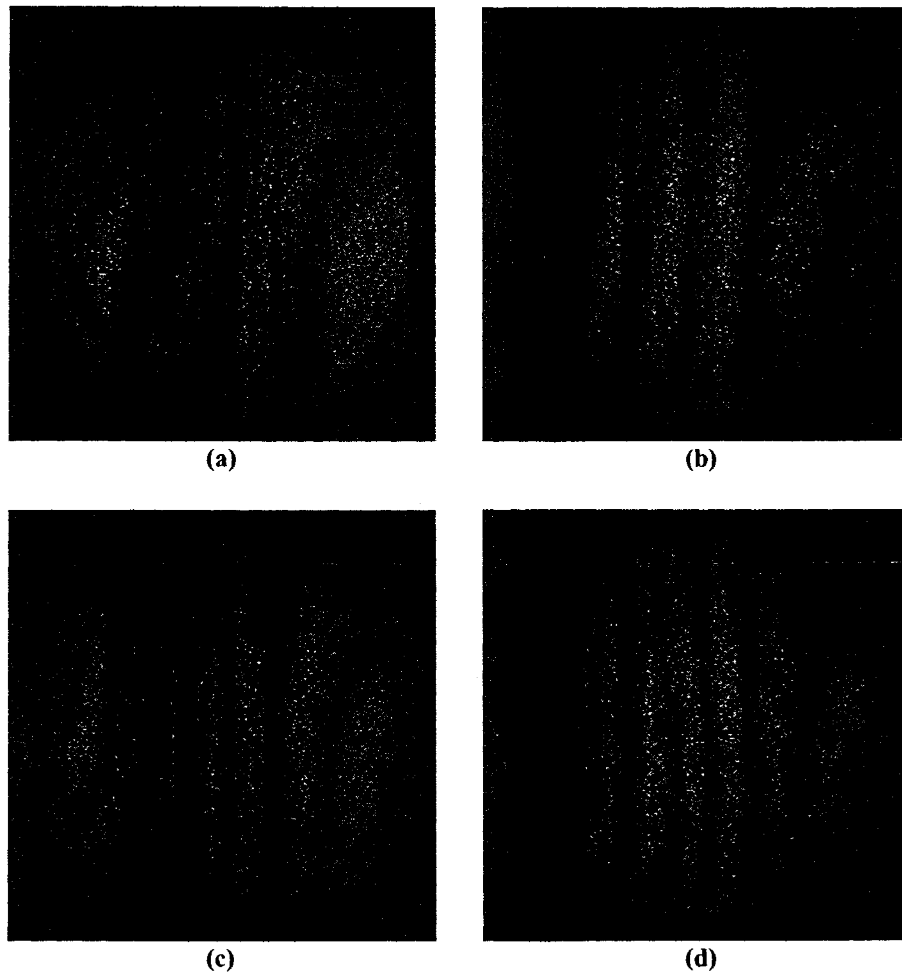

Figure 4.16 Fringe patterns of a perfect silicon wafer (heated up to55°C (90seconds)) created through cooling down the wafer after (a) T=3s (b) T=6s (c) T=9s and (d) T=12s

For crack detection in this work, the wafer started to crack due to fixturing. First, the cracked wafer was tested with thermal loading. The resulting fringe patterns have been shown in Figure 4.17.

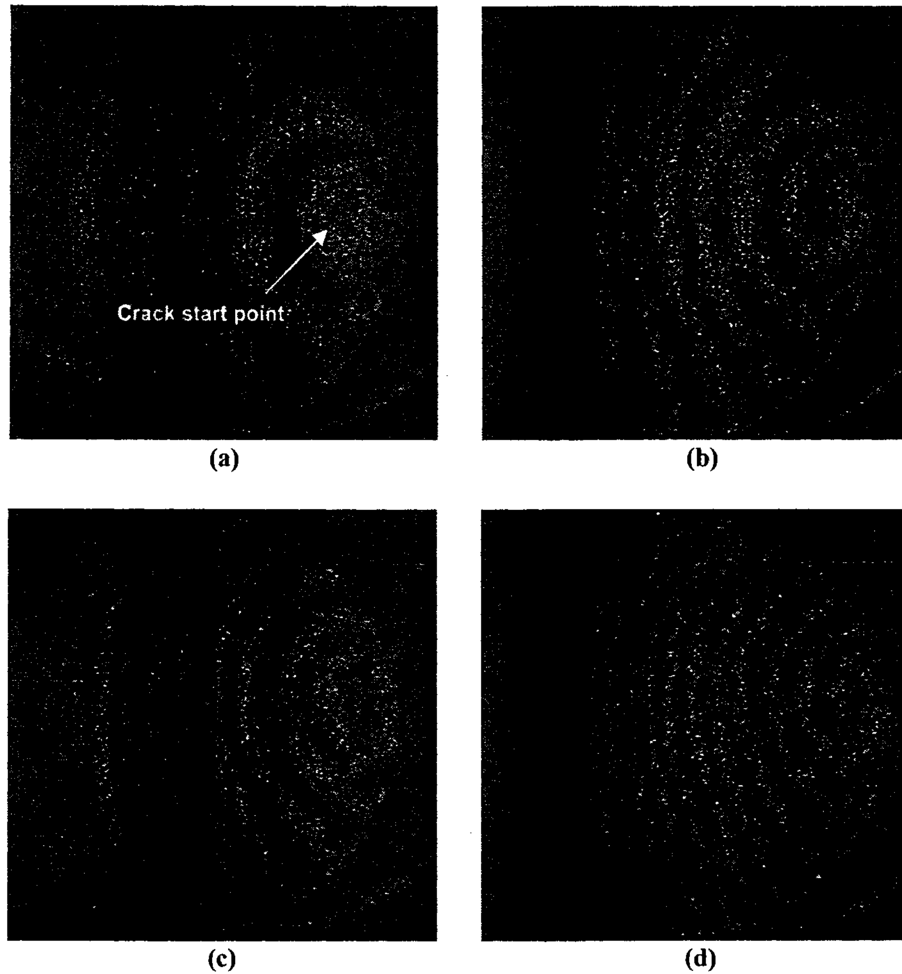

Figure 4.17 Fringe patterns of a cracked silicon wafer(heated up to55°C (90seconds)) created through cooling down the wafer after (a) T=3s (b) T=6s (c) T=9s (d) T=12s

Edge cracks cause the elliptical fringe patterns and the centre of the fringe curvature focuses on their start point, while surface cracks cause the fringe discontinuity areas on the fringe pattern. The mentioned defected wafer was also inspected with mechanical loading and the resulting fringe patterns have been shown in Figure 4.18.

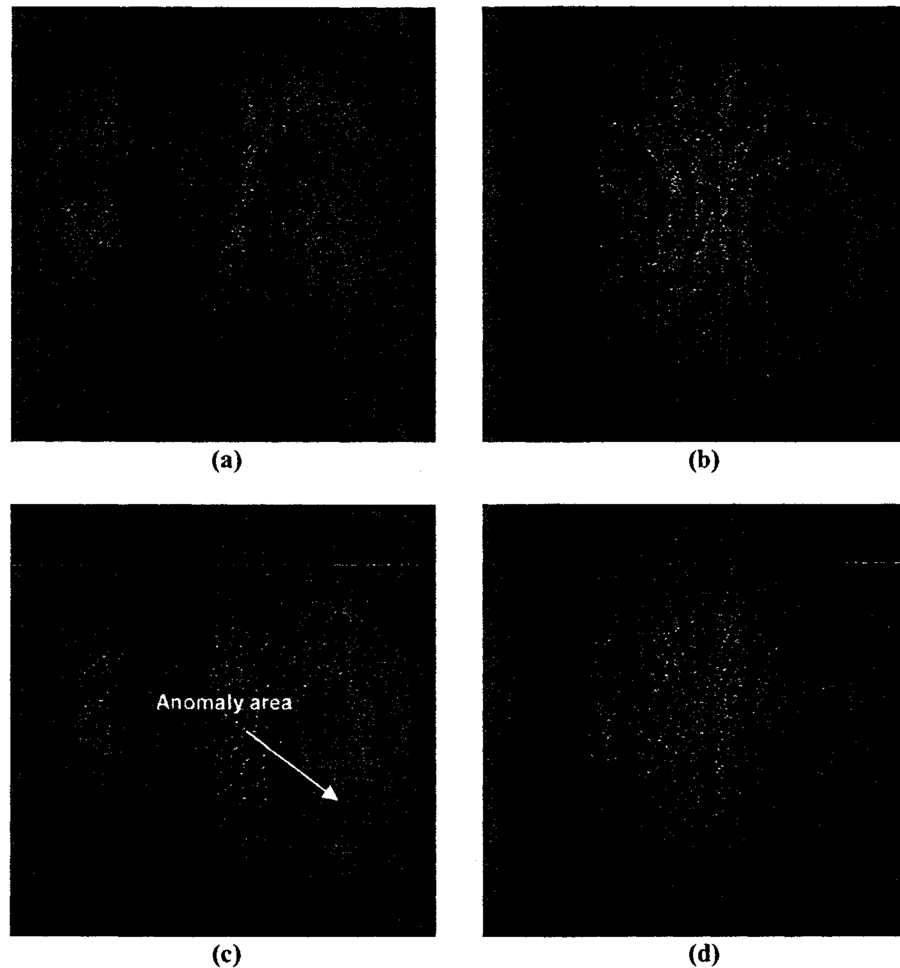

Figure 4.18 Fringe patterns of a cracked wafer obtained by concentrate-force loading through center-displacement of the silicon wafer: (a) 2μm displacement (b) 6μm displacement (c) 10μm displacement (d) 14μm displacement

As it can be seen, the cracks only appear as a fringe anomaly on the corners. Mechanical loading can not stimulate considerably the defective areas in the way that the strain concentration areas appear clearly on the fringe pattern.

As a continuation to the experiment on silicon wafer, in the third trial when the same wafer was heated up to 60°C (120seconds), the crack has completely propagated through the thickness and fringe patterns in Figure 4.19 shows the broken wafer. As it can be

seen, the smaller part of the wafer is completely separated from the whole wafer and there is no fringe pattern on it.

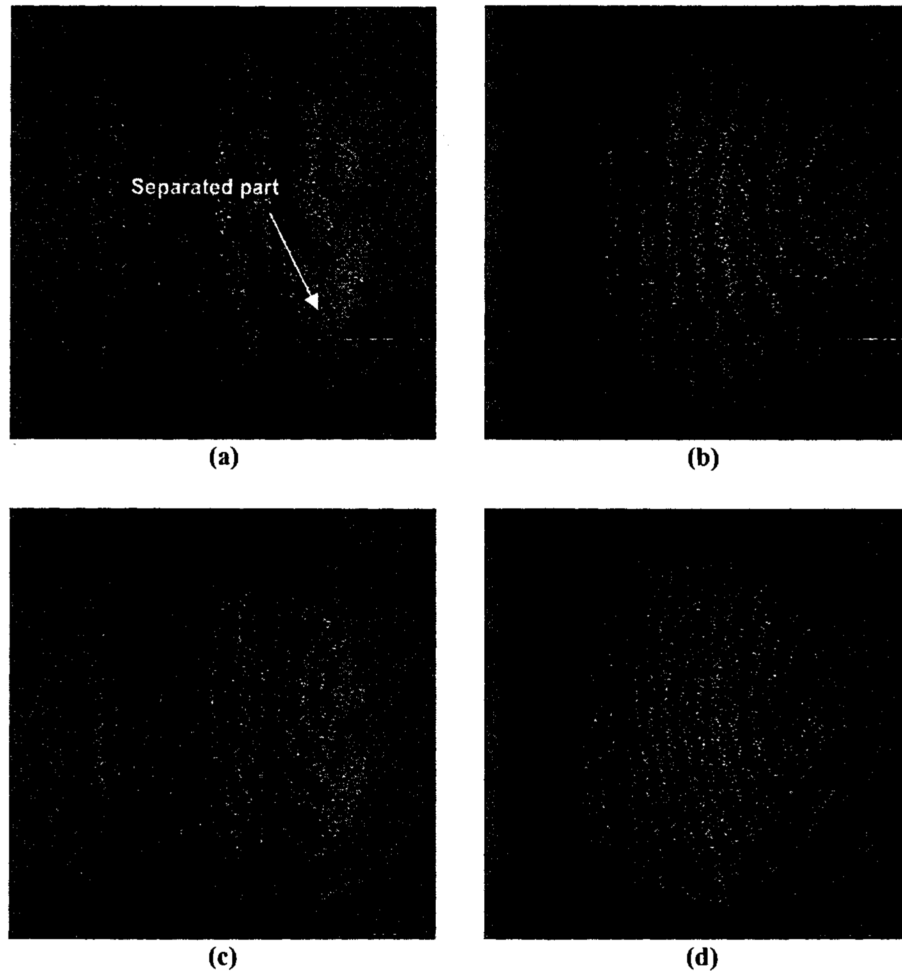

Figure 4.19 Fringe patterns of a broken silicon wafer (heated up to60°C (120seconds)) created through cooling down the wafer after (a) T=3s (b) T=6s (c) T=9s (d) T=12s

Effect of concentrate-force loading on crack detection: As shown in Figure 4.20, a (100) silicon wafer fracture happens usually along <110> directions on the surface which are inclined at 54.7° with respect to the wafer surface [80]. So, as can be seen in the cross section of the fracture area, while using concentrate-force loading, the broken parts of the wafer will support each other if the loading is applied from the directions shown in red.

Considering the probability of applying load in these situations, the whole wafer will bend at the same configuration in these cases and so, the strain concentration area cannot appear clearly as that of thermal loading.

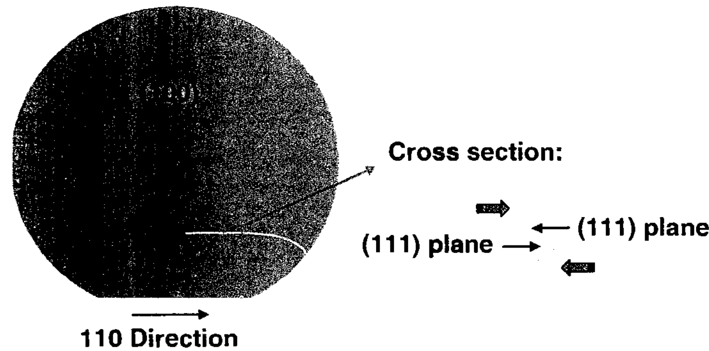

Figure 4.20 Schematic of the fracture angle in a (100) silicon wafer

While studying the broken wafer after the experiment, it was also observed that the crack had propagated along <110> direction. Hence, as explained earlier, the unsuitability of using concentrate-force loading for crack detection can be realized

4.3.2 Extension for crack propagation detection in silicon wafers

For industry applications, in case of using the live fringe correlation software, the crack propagation in wafer and breakage can be seen as a continuous process. So by applying the real amount of the thermal stress during processing, the mechanical stability of the wafer can be tested.

Using a live fringe processor allow to produce the fringe patterns continuously during heating up the wafer from appearing a crack on its edge to its breakage. In this type of

processing, a reference image (speckle pattern) is stored and the consequencing images are subtracted from the reference one and so, the fringe pattern will be recorded directly. By the exact start of the loading the object, a speckle pattern is recorded and it is considered as the reference image. Live fringe processing due to its much higher speed of generating the fringes is of more interest to be used in industrial applications [81].

Considering the real amount of thermal stress which is applied on the silicon wafer during its thermal processing, the duration and temperature range of the optical profile, which is applied for thermal loading the wafer, can be determined. The advantage of optical heating the wafer is that the applied thermal stress is uniform on the wafer surface and through its thickness. So, all the surface and sub-surface cracks and defects in any direction and position can be stimulated and show themselves as anomalies areas on the fringe patterns.

4.3.4 Sub-surface defect detection in silicon wafers

The sub-surface defects appear as bull's-eyes and unexpected fringe curvature and density changes. The same procedure that was used for crack detection on silicon wafers has been used in this part to detect sub-surface defects. Among the 10 wafers that were tested for sub-surface defect detection, only one of them was found to have a probable sub-surface defect. As it has been shown in Figure 4.21, increasing the fringe orders shows the position of sub-surface defect more accurately.

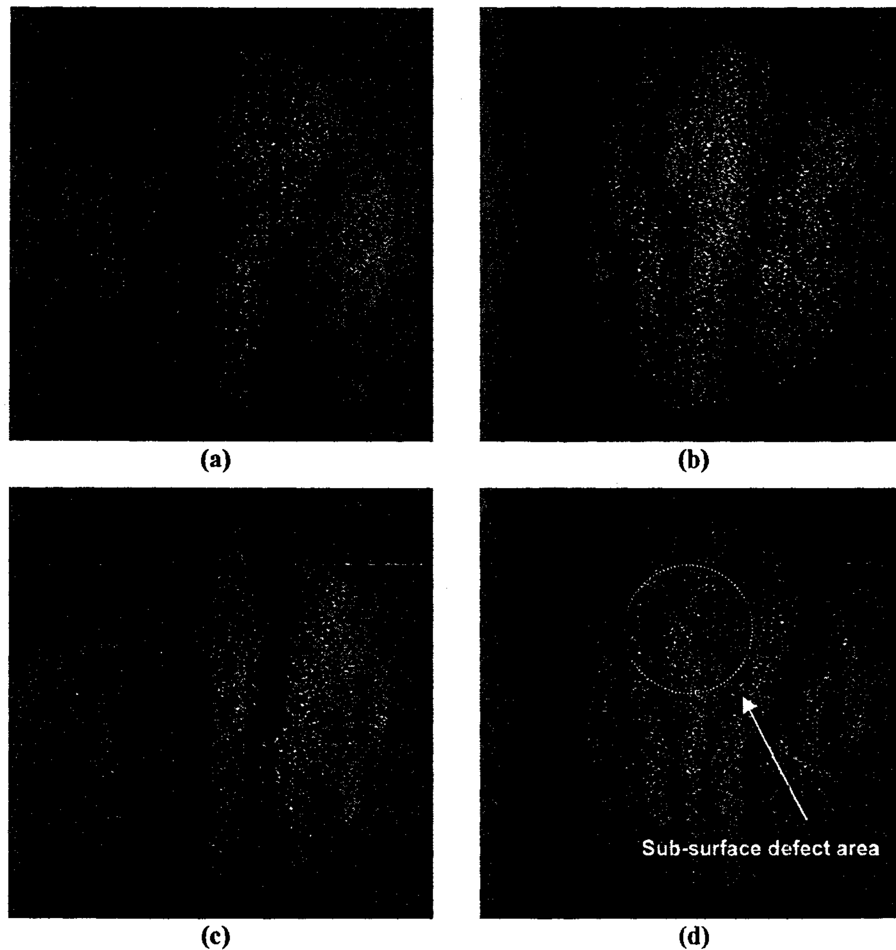

Figure 4.21 Fringe patterns of a silicon wafer (heated up to55°C (90seconds)) created through cooling down the wafer after (a) T=3s (b) T=6s (c) T=9s and (d) T=12s

Since polished wafers were used in the experiment, the probability of finding the sub-surface defects in the wafers compare to Ganesha's works [27] in which unpolished wafers were tested, was very low.

The advantage of thermal heating when compared with concentrated mechanical loading is that at the same time of the crack detection the sub-surface defects can also be detected. After determining the position of the critical defects, if there is a need to find out their exact size and depth for further processing, such methods that are able to inspect

the wafer locally in the defect position can be used . Then, the defective wafer may be sent for chemical mechanical machining and processed in order to be changed to a perfect wafer for production line.

4.4 Summary

In this chapter, first the experiments performed to optimize the performance of the shearography set-up were described and discussed. In this procedure, the optimal speckle size was chosen and the appropriate range of applying displacement in order to achieve fringe patterns was obtained. Higher quality fringe patterns also obtained through new arrangement of the set-up. Second, the experiments to investigate the crack detection in silicon wafers were carried out and promising results were achieved. The ability of the system to detect the crack on the wafer until its breakage was shown and its potential to be used for crack propagation detection was explained. Sub-surface defect detection was also achieved through the same procedure used for crack detection and the capability of the system to detect both crack and sub-surface defect was proved.

Chapter 5 Conclusion

5.1 Conclusion

Inspection methods used for defect detection in silicon wafers were reviewed in this work. Considering the limitations and disadvantages of the previous used methods and the importance of the crack detection in the new thin wafers, shearography technique was identified for NDE of the silicon wafers. Though shearography has been used for sub-surface defect detection in silicon wafers in 2004, there is no report on utilizing this technique for crack detection in silicon wafers. Since the objective of this work is to test the feasibility of shearography for crack detection in silicon wafers, the theory of this technique was explained and its application for non-destructive evaluation of different materials was reviewed.

As the first step of this research, a compact shearography system has been setup. A diode laser is used for the illumination system and a CCD camera combined to an imagining lens is utilized to image the interferograms through the shearing head. To avoid the external vibrations, all the components of the optical set-up are fixed on a vibration isolation table. Due to the short recording time, the influence of air turbulence and time-dependent disturbances are small and the designed system is relatively insensitive to the environmental ambient noise.

To optimize and check out the performance of the optical set-up, several experiments were carried out. To choose the optimum speckle size, different materials with different

surface properties were analyzed and the optimum ratio between the CCD cell size and speckle size was chosen to be 3:1. To show the capability of the system for different materials, a composite sample was also tested and the resulting fringe patterns were shown.

In order to increase the fringe visibility and get high order of fringes, the set-up was arranged for an out-of-plane displacement gradient measurement. The reliability of the set-up was checked with the theoretical model and the comparison between the experimental and theoretical results was discussed. The small angle of illumination and the imperfect bending of the wafer reduce the accuracy of resulting patterns. However, the fringe visibility improved considerably in order to perform a qualitative evaluation on silicon wafers which is the purpose of this research.

As the aim of this research, defect detection in silicon wafers was performed using the shearography set-up. Through optical heating the wafer surface, the imperfect areas appear as anomaly areas on the fringe pattern. Crack detection, which has not been done before by shearography, was done and promising results were achieved. By applying thermal stress on the wafer, the critical cracks appear as discontinuity on the fringe pattern and crack propagation could be inspected by performing a live fringe processing. Thermal loading and concentrate-force loading the wafer for crack detection were also compared and the suitability of the thermal loading was proved. Critical sub-surface defects can also be detected through thermal stressing the wafer and so by using shearography these two common types of defects in thin silicon wafers can be detected at

the same time. By using shearography, applying the same stress that the wafer will experience in the real process will help to determine the weak and unstable wafers before the production line.

5.2 Future works

Theoretical study of the behavior of the cracks and simulation of different testing conditions, considering the real situations in industrial processing needs to be performed in order to identify critical conditions.

To have more accurate results and also to find out the dimensions and exact position of the defects, there is a need to use phase shifting methods for fringe analysis. As the future work for this research, the first step is to arrange a phase shifting set-up for the shearography system in order to detect both cracks and sub-surface defects quantitatively.

The thermal loading is a simple method which is used in the proposed system for loading the wafer. To find the most appropriate type of loading for detection of different types of defects, it is necessary to study and investigate the other loading methods and assemble the most practical loading equipment in order to achieve an applicable NDT system for wafer inspection. In the future works of this research, it is supposed to investigate and compare the effect of thermal, vacuum and vibrational loadings in the shearography technique.

REFERENCES

[1] W Dallas, O Polupan, S Ostapenko, *Resonance ultrasonic vibrations for crack detection in photovoltaic silicon wafers*, Measurements Science and Technology 18 (2007)pp 852-858

[2] A. Belyaev, O polupan, W Dallas, S Ostapenko,D. Hess, *Crack detection and analysis using resonance ultrasonic vibrations in full-size crystalline silicon wafers*, Applied Physics Letters 88 (2006) 111907

[3] W. Murray Bullis, *Current trends in silicon defect technology*, Materials Science and Engineering B72 (2000) pp 93-98

[4] S. H. Wang, C.G. Quan, C. J. Tay, and H. M. Shang, *Surface roughness measurement in the submicrometer range using laser scattering*, Opt. Eng. 39 (2000) pp 1597-1601

[5] Akira Okamoto, Hitoshi Kuniyasu, and Takeshi Hattori, *Detection of 30-40nm particles on Bulk-Silicon and SOI wafers using Deep UV laser scattering*, IEEE Transactions on semiconductor manufacturing 19 (2006) NO. 4

[6] http://www.micromagazine.com/archive/05/08/bunday.html

[7] A.V. Frantskevich1, A.M. Saad, A.K. Fedotov, E.I. Rau, A.V. Mazanik and N.V. Frantskevich, *SEM investigation of surface defects arising at the formation of a buried nitrogen-containing layer in silicon*, Solid State Phenomena 131-133 (2008) pp 195-200

[8] Ishii Hiroyuki, Shiratake Shigeru, Oka Kazuhiro, Motonami Kaoru, Koyama Toru and Izumitani Junko, *Direct Observation of Crystal-Originated Particles on Czochralski-Grown Silicon Wafer Surface and Effect on Gate Oxide Reliability*, Japanese journal of applied physics. 35 (1996) pp L1385-L1387

[9] Morimasa Miyazaki, Sumio Miyazaki, Yoshio Yanase, Takashi Ochiai and Tatsuhiko Shigematsu, *Microstructure Observation of "Crystal-Originated Particles" on Silicon Wafers*, Japanese journal of applied physics. 34 (1995) pp 6303-6307

[10] Albrecht, T.R., Akamine, S., Carver, T.E., and Quate, C.F., *Microfabrication of cantilever styli for the atomic force microscope,* J. Vac. Sci. Technol. A 8(4) (1990) pp 3386-3396

[11] T. Kobayashi, I. Uchiyama, A. Kimura, S. Oka, Y. Kitagawara, *Direct observation of electrically harmful surface defects of Si wafer immersed in slightly Cu-contaminated water*, Journal of Crystal Growth 210 (2000) pp 112-115

[12] T. Nishimura, S. Wakiyama, M. Yasutake, and Y. Sugano, *Defect observation on a 12-in silicon wafer using large sample atomic force microscopy*, J. Vac. Sci. Technol. (2000) B 18(3)

[13] *High Resolution X-ray Diffractometry and Topography*, by D. Keith Bowen and Brian K. Tanner, Taylor & Francis, Ltd., 1998 (Semiconductors and thin film analysis)

[14] Seiji Kawado, *X-ray characterization of crystal perfection and surface contamination in large-diameter silicon wafers*, Materials Science in Semiconductor Processing 5 (2003) pp 435-444

[15] Ishikawa T, Kohra K In: *Handbook on synchrotron radiation*, vol. 3. Amsterdam: Elsevier, 1991. [Chapter 3]

[16] Metals and Ceramics Division, Oak Ridge National Laboratory: http://www.html.ornl.gov/mituc/sam2000.htm

[17] A Belyaev, O Polupan, S Ostapenko, D Hess and J P Kalejs, *Resonance ultrasonic vibration diagnostics of elastic stress in full-size silicon wafers*, Semicond. Sci. Technol.21 (2006) pp 254-260

[18] http://www.edevis.de/thermography/Ultraschall_Lockin_Thermografie_en.php

[19] Rakotoniaina J P, Breitenstein O, Al Rifai M H, Franke D and Schnieder A, *Detection of cracks in silicon wafers and solar cells by lock-in ultrasound thermography*, Proc. PV Solar Conf. (Paris, June) (2004) pp 640–3

[20] Rueland E, Herguth A, Trummer A, Wansleben S and Fath P, *Optical μ-crack detection in combination with stability testing for in-line inspection of wafers and cells*, Proc. 20th EU PVSEC (Barcelona, June) (2005) pp 3242–5

[21] Bai Weimin, Brian Stephen Wong and Murukeshan V M, *Thermographic and Laser Shearographic Evaluation of composite materials*, NDT.net 8 (2003) No.2

[22] Ulf Schnars and Werner Jueptner, *Digital Holography: Digital Hologram Recording, Numerical Reconstruction, and Related Techniques*, Springer (2004)

[23] Thomas et al., *Direct to Digital Holography for Semiconductor Wafer Defect Detection and Review, Design, Process Integration, and Characterization for Microelectronics*, Proceedings of SPIE 4692 (2002) pp 180-194

[24] Schulze, M. A. Hunt, M. A. Voelkl, E. Hickson, J. D. Usry, W. R. Smith, R. G. Bryant and R. Thomas, C. E., *Semiconductor wafer defect detection using digital holography*, Proceedings- SPIE The International Society for Optical Engineering ISSU 5041 (2003) pp 183-193

[25] P. K. Rastogi, *Digital speckle pattern interferometry and related techniques*, Wiley (2001)

[26] Wolfgang Steinchen, *Digital Shearography: Theory and Application of Digital Speckle Pattern Shearing Interferometry*, SPIE-International Society for Optical Engine (2003)

[27] Udupa Ganesha, Ngoi B. K. A., Goh H. C. Freddy and Yusoff M. N., *Defect detection in unpolished Si wafers by digital shearography*, Meas. Sci. Technol. **15** (2004) pp 35-43

[28] Leendertz J.A. and Butters J.N., *An image-shearing speckle-patterns interferometer for measuring bending moments*, J. Phys. E, 6 (1973) pp 1107-1110

[29] Hung Y.Y., *Shearography, a new optical method for strain measurement and nondestructive testing*, Opt. Eng., 21 No. 3 (1982) pp 391-395

[30] S. L. Toh, H. M. Shang, F. S. Chau, C. J. Tay, *Flaw detection in composites using time-average shearography*, Optics & Laser Technology, 23 No. 1(1991) pp 25-30

[31] S. L. Toh, F. S. Chau, V. P. W. Shim, C. J. Tay, H. M. Shang, *Application of shearography in nondestructive testing of composite plates*, Journal of Materials Processing Technology, 23 (1990) pp 267-275

[32] L. X. Yang, W. Steinchen, M. Schuth, G. Kupfer, *Precision measurement and nondestructive testing by means of digital phase shifting speckle pattern and speckle pattern shearing interferometry Measurement*, Measure.-J. Intl. Measure. Confed. 16 (1995) pp 149-160

[33] W. Steinchen, L. X. Yang, M. Schuth, G. Kupfer, *Application of shearography to quality assurance*, Journal of Materials Processing Technology, 52 (1995) pp 141-150

[34] Hung. Y.Y., Rowlands R.E. and Daniel I.M., *Speckle-shearing interferometric technique: a full-field strain gauge*, Appl. Opt. 14 No. 3 (1975) pp 618-622

[35] Steinchen W., Yang L.X., Schuth M. and Kupfer G., *Electronic shearography (ESPSI) for direct measurement of strains*, Proc. SPIE 2248 (1994) pp 210-221

[36] C. W. Sim, F. S. Chau, S. L. Toh, *Vibration analysis and non-destructive testing with real-time shearography*, Optics & Laser Technology, 27 No.1 (1995) pp 45-49

[37] J. D. R. Valera, J. D. C. Jones, D. P. Towers and, C. H. Buckberry, *Strain and vibration analysis by fiber based speckle shearing interferometry*, Optics and Lasers in Engineering, 26 No.4-5 (1997) pp 361-376

[38] J. W. Goodman, *Statistical properties of laser speckle patterns: in laser speckle and related phenomena*, 2nc Edition, J. C. Dainty (Ed.), Springer-Verlag, Berlin, 1984

[39] Max Born and Emil Wolf, *Principles of Optics: electromagnetic theory of propagation, interference and diffraction of light*, Edition 7th expanded, New York, Cambridge University Press, 1999

[40] Sridhar Krishnaswamy, *Optical Methods of Inspecting Composites (Holography and Shearography)*, Comprehensive Composite Materials Chapter 5.19 (2003) pp. 447-468

[41] K. Creath, *Temporal phase measurement methods, in interferograms analysis*, D. W. Robinson and G. T. Reid (Eds), Institute of physics, Bristol, 1993

[42] M. Kujawinska, *Spatial phase measurement methods, in interferograms analysis*, D. W. Robinson and G. T. Reid (Eds), Institute of physics, Bristol, 1993

[43] W. Osten and W. Juptner, *Digital processing of fringe patterns in optical metrology: in optical measurement techniques and applications*, P.K. Rastogi (Ed.), Artech House, Boston, MA, 1997

[44] T. Yatagai, *Intensity based analysis methods, in interferograms analysis*, D. W. Robinson and G. T. Reid (Eds), Institute of physics, Bristol, 1993

[45] Bracewell R., *The Fourier Transform and Its Applications*, New York: McGraw-Hill (1999)

[46] Brigham E. O., *The Fast Fourier Transform and Applications*, Englewood Cliffs, NJ: Prentice Hall (1988)

[47] http://www.dantecdynamics.com/

[48] Alexis Lagarde, *Iutam Symposium on Advanced Optical Methods and Applications in Solid Mechanics*, Springer (2000)

[49] Y. Y. Hung, *Applications of digital shearography for testing of composite structures*, Composites Part B: Engineering 30 No. 7 (1999) pp 765-773

[50] Roman Růžek, Radek Lohonka and Josef Jironč, *Ultrasonic C-Scan and shearography NDI techniques evaluation of impact defects identification*, NDT & E International 39 No. 2 (2006) pp 132-142

[51] Xide Li, Xingfu Liu and Kai Wang, *Quantitative detection of the defects in thin-walled pressure vessels with holography and shearing speckle interferometry*, Journal of nondestructive evaluation 21 No. 3 (2002) pp 85-94

[52] Kyung-Suk Kim, Ki-Soo Kang, Young-June Kang and Seong-Kyun Cheong, *Analysis of an internal crack of pressure pipeline using ESPI and shearography*, Optics & Laser Technology 35 No. 8 (2003) pp 639-643

[53] Gryzagoridis J., Findeis D. and Schneider D. R., *The impact of optical NDE methods in vessel fracture protection*, International journal of pressure vessels and piping 61 No. 2-3 (1995) pp 457-469

[54] Fernando Santos, M.Mário Vaz and Jaime Monteiro, *A new set-up for pulsed digital shearography applied to defect detection in composite structures*, Optics and Lasers in Engineering 42 No 2 (2004) pp 131-140

[55] M. V. Rao, R. Samuel and A. Ananthan, *Applications of electronic speckle interferometry (ESI) techniques for spacecraft structural components*, Optics and Lasers in Engineering 40 No 5-6(2003) pp 563-571

[56] Narayan U. Sujatha and Vadake M. Murukeshan, *Nondestructive inspection of tissue/tissue like phantom curved surfaces using digital speckle shearography*, Optical Engineering 43 No.12 (2004) 3055-3060

[57] Ngoi B K A, Freddy Goh H C, Udupa G and Yusoff M N, *System and method for inspection of silicon wafers*, Patent pending No. 200300562-6 (2003) Singapore

[58] Mujeeb A, Ravindran VR and Nayar VU, *Application of ESPI for the NDE of low-modulus materials using mechanical loading*, Insight 49.1 (2007) pp 21-25

[59] M.H. Majles Ara and R.S. Sirohi, *Speckle interferometry methods for displacement and strain measurements using photorefractive crystal*, Optik 118 (2007) pp 445–451

[60] E. Mihaylova, B. Potelonl, S. Reddy, V. Toal and C. Smith, *Mechanical characterization of unplasticised polyvinylchloride thick pipes by optical methods*, Optics and Lasers in Engineering 41 (2004) pp 889–900

[61] Erwin Hack and Rolf BroK nnimann, *Electronic speckle pattern interferometry deformation measurement on lightweight structures under thermal load*, Optics and Lasers in Engineering 31 (1999) pp 213-222

[62] http://www.convergentlaser.com/

[63] Y.Y. Hunga and H.P. Hob, *Shearography: An optical measurement technique and applications*, Materials Science and Engineering R 49 (2005) pp 61–87

[64] Melles Griot , Manual book (1999)

[65] Spooren R., *Standard charge coupled device cameras for video speckle interferometry*, Optical engineering 33 (1994) pp 889-896

[66] R. Spooren, A. Aksnes Dyrseth and M. Vaz, *Electronic shear interferometry-application of a (double-) pulsed laser*, Appl. Opt. 32 (1993) pp 4719-4727

[67] W. Osten, F. Elandalousii and M. Stache, *Handbook of Fringe Evaluation*, Bremer Institut für angewandte Strahtechnik (1997-2000)

[68] Mette Owner-Petersen, *Decorrelation and fringe visibility: on the limiting behavior of various electronic speckle-pattern correlation interferometers*, Journal of the optical society of America A-Optics image science and vision 8 (1991) pp 1082-1089

[69] Takeaki Yoshimura, Minniu Zhou, Keiji Yamahai, and Zhang Liyan, *Optimum determination of speckle size to be used in electronic speckle pattern interferometry*, Applied Optics 34 (1995) pp 87-91

[70] Yasuhiko Arai, Shunsuke Yokozeki, *In-plane displacement measurement using electronic-speckle-pattern-interferometry-based on spatial fringe analysis method*, Optical Engineering 43 (2004) pp 2168-2174

[71] J. Burke, T Bothe, H Helmers, C. Kunze, R. S. Sirohi, V. Wilkens, *Spatial Phase shifting in ESPI: Influence of second-order Speckle Statistics on Fringe Quality*, Carl von Ossietzky Universitat Oldenburg, FB Physic, Postfatch 2503, D-26111 Oldenburg

[72] Amalia Martínez, Ramón Rodríguez-Vera, J.A. Rayas and H.J. Puga, *Fracture detection by grating moiré and in-plane ESPI techniques*, Optics and Lasers in Engineering 39 (2003) pp 525–536

[73] A. Davilaa, P.D. Ruizb, G.H. Kaufmannb and J.M. Huntleya, *Measurement of sub-surface delaminations in carbon fibre composites using high-speed phase-shifted speckle interferometry and temporalphase unwrapping*, Optics and Lasers in Engineering 40 (2003) pp 447–458

[74] Lianxiang Yang, Ping Zhang, Sheng Liu, Praveen R. Samala, Min Su and Hiroki Yokota, *Measurement of strain distributions in mouse femora with 3D-digital speckle pattern interferometry*, Optics and Lasers in Engineering 45 (2007) pp 843–851

[75] Murali M. Pai S, *Acousto optic modulated stroboscopic interferometer for comprehensive characterization of microstructure*, PhD Thesis, Concordia University (2008)

[76] Budynas and Richard G., *Advanced strength and applied stress analysis*, Boston WCB/McGraw-Hill (1999)

[77] C.C. Chao, R. Chleboski, E.J. Henderson, C.K. Holmes, J.P. Kalejs and T.S. Gross, *Fracture behavior of silicon with a high power laser*, Mat. Res. Soc. Symp. Proc. 226, (1991) 363

[78] Sopori B, Sheldon P and Rupnowski P, *Wafer breakage mechanism(s) and a method for screening 'problem wafers'*, 16th Workshop on Crystalline Silicon Solar Cells and Modules (2006)

[79] Behnken H, Apel M and Franke D, *Simulation of mechanical stress during bending tests for crystalline wafers*, 3rd World Conf. on Photovoltaic Energy Conversion (2003)

[80] Nadim Maluf and Kirt Williams, *An Introduction to microelectromechanical systems engineering–2nd ed.*, Artech HouseOUSE INC. (2004)

[81] Holography for the New Millennium, Chpater 9: *Holography and Speckle Techniques Applied to Nondestructive Measurement and Testing*, Springer (2002)

APPENDIX 1

- Al surface: Ra = 1.13μm

Veeco **3-Dimensional Interactive Display**

Date: 07/28/2008
Time: 15:26:29

Surface Stats:
Ra: 1.13 um
Rq: 1.45 um
Rt: 12.85 um

Measurement Info:
Magnification: 10.01
Measurement Mode: VSI
Sampling: 989.17 nm
Array Size: 640 X 480

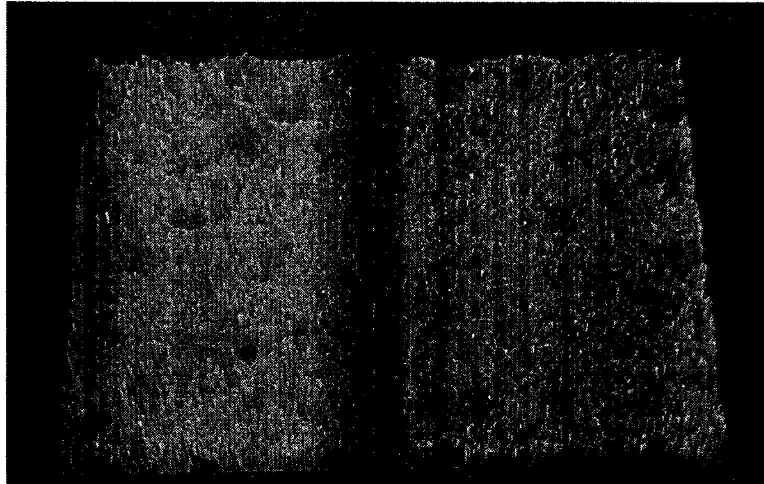

- Carbon composite painted surface: Ra = 3.65 μm

Veeco **3-Dimensional Interactive Display**

Date: 07/28/2008
Time: 15:16:49

Surface Stats:
Ra: 3.65 um
Rq: 4.34 um
Rt: 24.22 um

Measurement Info:
Magnification: 1.23
Measurement Mode: VSI
Sampling: 8.06 um
Array Size: 640 X 480

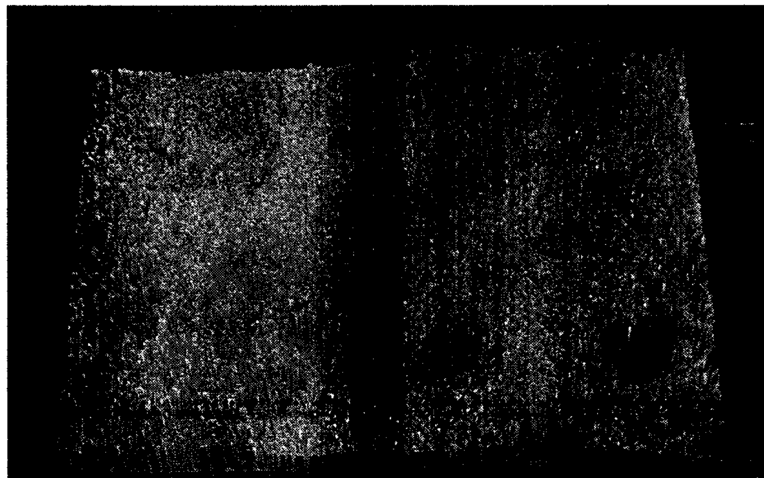

Silicon wafer surface roughness

- Silicon wafer polished surface: Ra = 5.89nm

Veeco 3-Dimensional Interactive Display

Date: 07/28/2008
Time: 15:06:40

Surface Stats:
Ra: 5.89 nm
Rq: 7.42 nm
Rt: 121.11 nm

Measurement Info:
Magnification: 1.23
Measurement Mode: PSI
Sampling: 8.06 um
Array Size: 640 X 480

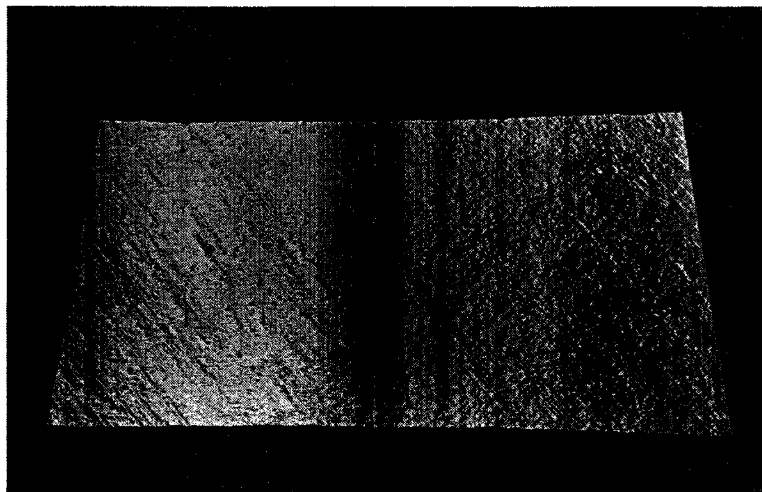

- Silicon wafer unpolished surface: Ra = 686.52nm

Veeco 3-Dimensional Interactive Display

Date: 07/28/2008
Time: 15:03:23

Surface Stats:
Ra: 686.52 nm
Rq: 880.72 nm
Rt: 9.47 um

Measurement Info:
Magnification: 1.23
Measurement Mode: VSI
Sampling: 8.06 um
Array Size: 640 X 480